Arabian Journal of Geosciences (2024) 17:9
https://doi.org/10.1007/s12517-023-11766-7

ORIGINAL PAPER

New insights into the ultrapotassic magmatism through xenoliths from the Eğirdir area, West Anatolia, Turkey

Platevoet Bernard[1] · Bardintzeff Jacques-Marie[1] · Elitok Ömer[2] · Noret Aurélie[1] · Grégoire Michel[3] · Poisson André[1]

Received: 14 July 2023 / Accepted: 28 October 2023 / Published online: 8 December 2023

Abstract
Plutonic xenoliths have been found within a pipe and a related phreatomagmatic leucitite deposit in the Eğirdir lake area, belonging to the Potassic-Ultrapotassic Afyon volcanic Province, West Anatolia. They consist of kamafugite-type, feldspar-bearing syenite, pyroxenite, leucitolite, some small-sized melilitolite and garnet-rich xenoliths, and a carbonatite. A new occurrence of kalsilite is described as either homogeneous acicular crystals or tabular two phases-exsolved crystals in the kamafugite-type and melilitolite xenoliths. Rock textures and compositions indicate cumulates and near-liquid composition rocks corresponding to relatively evolved magmas. All the rocks are strongly silica-undersaturated, Ca-, Mg-, and K-rich, and Al-poor. The fractional crystallization model includes clinopyroxene, apatite, phlogopite, melilite and leucite. Fe-Ti oxides and garnet may be also concerned. The P_{H2O} during crystallization and differentiation is not more than 0.8 GPa. Major elements, trace elements, and REE patterns for xenoliths, which indicate near-liquid compositions, are typical of ultrapotassic series in a post-collisional geodynamic context, as it is the case for the Roman and Central ultrapotassic Italian provinces. The stable isotope ^{13}C and ^{18}O values of the calcio-carbonatite plot close to the primary carbonatite field, whereas the carbonates of the feldspar-bearing syenite and the peperite matrix suggest a low-T extensive contamination process. The origin of the carbonatite from kamafugite-type magmas by immiscibility or by fractional crystallization remains questionable; an origin by fractionation-melting of a metasomatized mantle source should be tested in the future.

Keywords Ultrapotassic rock · Kamafugite · Leucitolite · Carbonatite · Turkey

Introduction

New occurrence of strongly silica-undersaturated, potassic-ultrapotassic plutonic xenoliths

We report here the mineralogy and geochemical data for a new occurrence of melilite-, leucite-, kalsilite-bearing plutonic xenoliths found in the southern part of the Potassic-Ultrapotassic Afyon Province, Turkey. Some rare occurrences of such plutonic rocks have been previously found for example in the ejectas from Alban Hills and Montefiascone volcanism, Italy (Keller 1983; Peccerillo et al. 1984; Federico et al. 1994; Vollmer 1989; Beccaluva et al. 1991; Beccaluva et al. 2012; Peccerillo 1990, 1992, 1994; Di Battistini et al. 2001; Stoppa 2003; Stoppa et al. 2003a; Gaeta et al. 2006; Conticelli et al. 2013, 2015), and also in the ultrapotassic volcanic series from the East African rift (Bell and Powell 1969; Mitchell and Bell 1976; Pouclet 1980; Edgar and Arima 1981; Bergman 1987; Kampunzu and Lubala 1991; Laval and Hottin 1992; Bell and Tilton 2001; Stoppa

---

This work is dedicated to the late Dr. A. Poisson who have shown the studied area to the first author many years ago.

Responsible Editor: Domenico M. Doronzo

✉ Bardintzeff Jacques-Marie
jacques-marie.bardintzeff@universite-paris-saclay.fr

Platevoet Bernard
bernard.platevoet@orange.fr

Elitok Ömer
oelitok@gmail.com

Noret Aurélie
aurelie.noret@universite-paris-saclay.fr

Grégoire Michel
michel.gregoire@get.omp.eu

[1] UMR CNRS 8148 GEOPS, Université Paris-Saclay, Géosciences, GEOPS, Bât. 504, 91405 Orsay, France

[2] Department of Geological Engineering, Süleyman Demirel University, 32260 Isparta, Turkey

[3] Géosciences Environnement, Toulouse, CNRS-CNES-IRD, Observatoire Midi-Pyrénées, 14 A. E. Belin, 31400 Toulouse, France

et al. 2003b). For a long time, authors have paid attention to the distinctive mineralogy of potassic-ultrapotassic rocks in relation with magma crystallization and differentiation (Yoder 1986; Veksler et al. 1998) and their complex hypothetic mantle source and successive mantle metasomatism events in relation with a post-collision, extensional geodynamical context (Savasçin et al. 1994; Yağmurlu et al. 1997). However, there are few data regarding plutonic intracrustal intrusions especially for the tertiary Potassic-Ultrapotassic Afyon volcanic Province. Erosion processes did not allow access to the plutonic level, and only scarce mafic–ultramafic xenoliths entrained during volcanic events have been described and related to crustal intrusions (Akal 2003; Prelević et al. 2015).

Geological background

As part of the Alpine-Himalayan orogenic belt, Turkey consists of an amalgamation of Gondwana-derived continental blocks associated with ophiolitic units. The Anatolide-Tauride block which occupies western and southern parts of Turkey is subdivided into zones based on the type of metamorphism and age of deformation (Fig. 1a, b): Tavşanlı Zone, Afyon Zone, Menderes Massif, Bornova Flysch Zone, and Tauride Belt. The first four zones are characterized by medium–high-pressure metamorphic rocks (Bornova Flysch Zone). These zones are the low-grade metamorphic basement intruded by felsic igneous rocks (Tauride Belt, Gürsu et al. 2004), Mesozoic to Cenozoic sedimentary sequences, and stack of imbricated, ophiolite-bearing allochthonous nappes. The western part of the Tauride carbonate axis forms a north-pointing cusp in the north of Eğirdir Lake, the so-called Isparta Angle, and includes the study area. The northeast–southwest trending Beydağları platform carbonate separates allochthonous ophiolitic rock units with, from west to east, the Lycian nappes, the Antalya complex, and the Hoyran-Beyşehir-Hadım nappes. These four nappe systems join around Eğirdir Lake (Fig. 1b). Southwestern Turkey has been subjected to compressional and extensional tectonic activities, ophiolite emplacements, block rotations, and volcanic activities throughout Phanerozoic time.

Neotectonic structures developed in SW Turkey during the Late Miocene to Early Pliocene with local effects at the end of Middle Oligocene in a transtensional regime (Koçyiğit 1984a, b). They correspond to regional uplift, continental sedimentation (thick pile of molasse deposition), syn-sedimentary volcanism, and block faulting.

Potassic-ultrapotassic volcanisms in West Anatolia

North–south trending volcanic rocks, named Kırka-Afyon-Isparta Volcanic Province or Kırka-Afyon-Isparta Alkaline Volcanic assemblage (after Savaşçın and Oyman 1998), crop out from the apex of the Isparta Angle to the north of Afyon, including the studied area, and are characterized mainly by potassic–ultrapotassic volcanic rocks (Fig. 1a, c) (Alici et al. 1998; Akal 2003; Platevoet et al. 2008, 2014; Elitok 2019; Prelević et al. 2012, 2015; Akal et al. 2013). In general, from north to south in the Kırka-Afyon-Isparta volcanic Province, volcanic activities get younger: 14.8 and 8.6 Ma around Kırka-Afyon in the north, from 4.7 ± 0.2 Ma around Isparta (Lefèvre et al. 1983) to 24 ± 2 ka (Platevoet et al. 2008) and 12.9 ± 0.4 ka (Guillou et al. 2017) in the south, corresponding to the last volcanic events of the Gölcük volcano. The volcanic activities in SW Turkey are in close relationship with the neotectonic evolution of the region.

The Tertiary-Quaternary volcanic Province of West Anatolia is divided into a northern series named the Potassic-Ultrapotassic Afyon volcanic Province (Akal 2003; Akal et al. 2013; Prelević et al. 2012, 2015) extending north to south, from Afyon to Eğirdir Lake (Fig. 1b). It is formed by three main series, including a strongly silica-undersaturated, leucite-bearing volcanic series located at the southern part where we found the xenoliths, the subject of the present study. The Isparta potassic volcanic series is more recent, with the Quaternary Gölcük volcano situated in the so-called Isparta Angle (Lefèvre et al. 1983; Alici et al. 1998; Platevoet et al. 2008; Çoban et al. 2019).

Field occurrence

Sample locations are in the NW Hoyran lake (N Eğirdir lake), within a NE-SW trending horst structure bounded by the Senirkent graben in the south (Fig. 1c) and the Haydarli graben in the north. Mesozoic formations consisting mainly of massive or bedded limestones form the basement (Fig. 1c, d), locally unconformably overlain by Eocene flysch-type deposit, or by Upper Miocene-Pliocene volcano-sedimentary deposits (Elitok 2019, and references therein). Trachytic domes are observed in the west of the studied area and leucite-bearing lava dome flows are observed to the NW close to the Haydarli graben.

Along the Afyon-Karahisar road, the Cretaceous limestones and Cenozoic lacustrine levels are cut by a volcanic pipe 5 m wide (Fig. 1e). This pipe consists of a leucite-bearing brownish volcanic material including numerous xenoliths of volcanic and plutonic types. At the contact between the pipe and the limestone basement, the limestones are brecciated and some blocks are incorporated in the volcanoclastic breccia. The xenoliths and the enclosing matrix are extensively hydrothermally altered by a CO_2-dominant fluid phase, as evidenced by millimeter- to centimeter-size calcite veins.

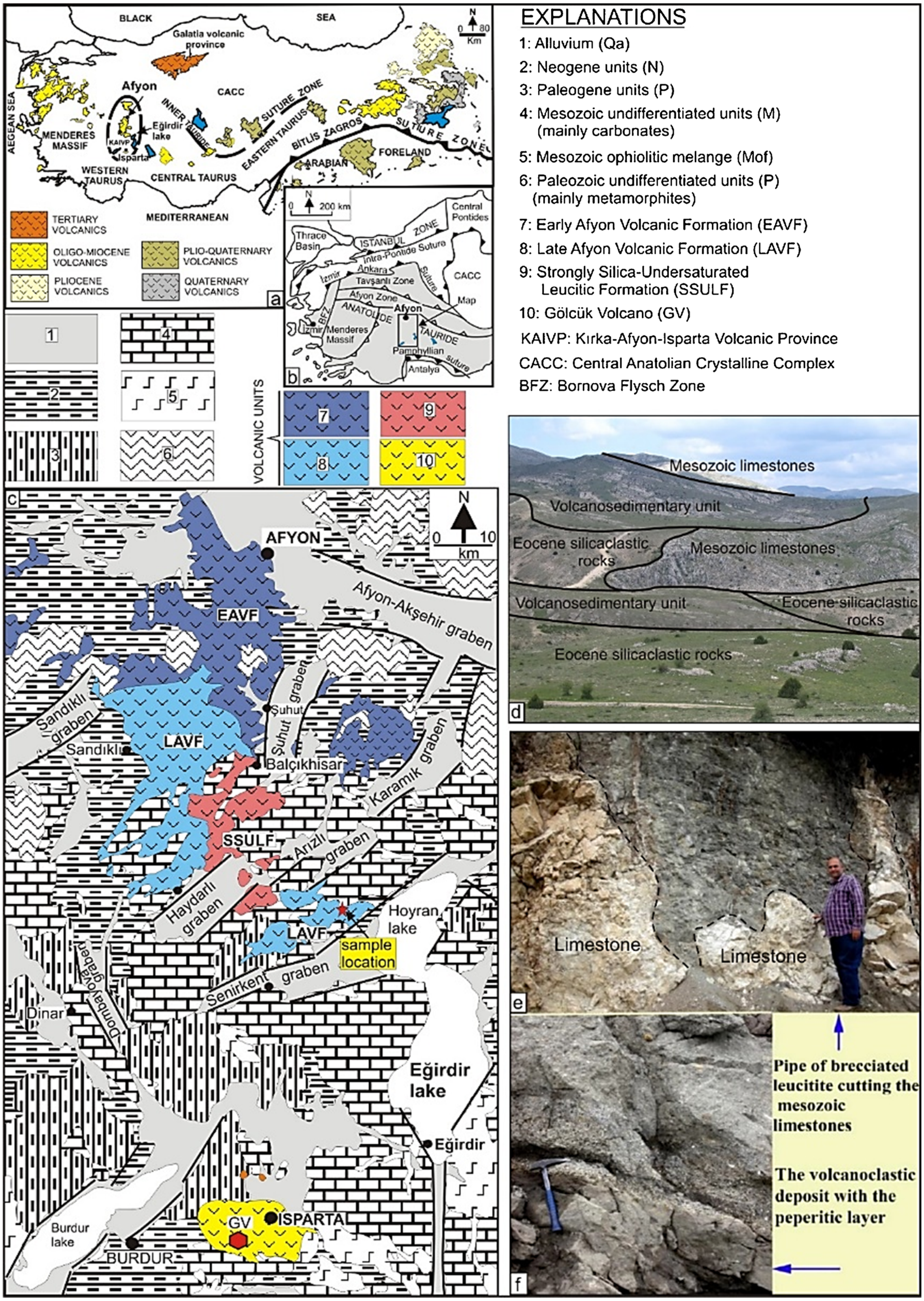

Fig. 1 Geographic situation and geological map. Localization of the studied area and geological map from Isparta to Afyon northwest of Egirdir Lake, Anatolia: **a** volcanics in Anatolia; **b** structural scheme of West Anatolia; **c** main geological units from Afyon to Isparta; **d** local geological units near the studied area; **e** top, the leucitite pipe with limestone blocks and xenoliths; **f** the volcanoclastic deposit, the peperite has a white calcitic matrix including black leucitite granules

Near the pipe, towards the south, a volcanoclastic deposit is formed by a brecciated leucitite, which also contains numerous xenoliths. The lower part of this volcanoclastic deposit is composed of a 50-cm-thick layer of a pulverized leucitite lava in a calcitic-zeolitic matrix, similar to a peperite (Fig. 1e, f). The xenoliths (5 to 20 cm in size) were collected in this volcanoclastic deposit. They are angular or rounded and show a variety of textures from fine-grained porphyric textures to equant coarse-grained textures (Fig. 2). The xenoliths are leucocratic to melanocratic, depending on their mafic-felsic mineral assemblage. Small ultramafic xenoliths (no more than 5 cm in size) and a single coarse-grained carbonatite xenolith (10 cm in size) were also found. The xenoliths are relatively well preserved from hydrothermal alteration and provide a good opportunity for a petrological study in order to specify their possible connection with the Potassic Ultrapotassic Afyon volcanic Province.

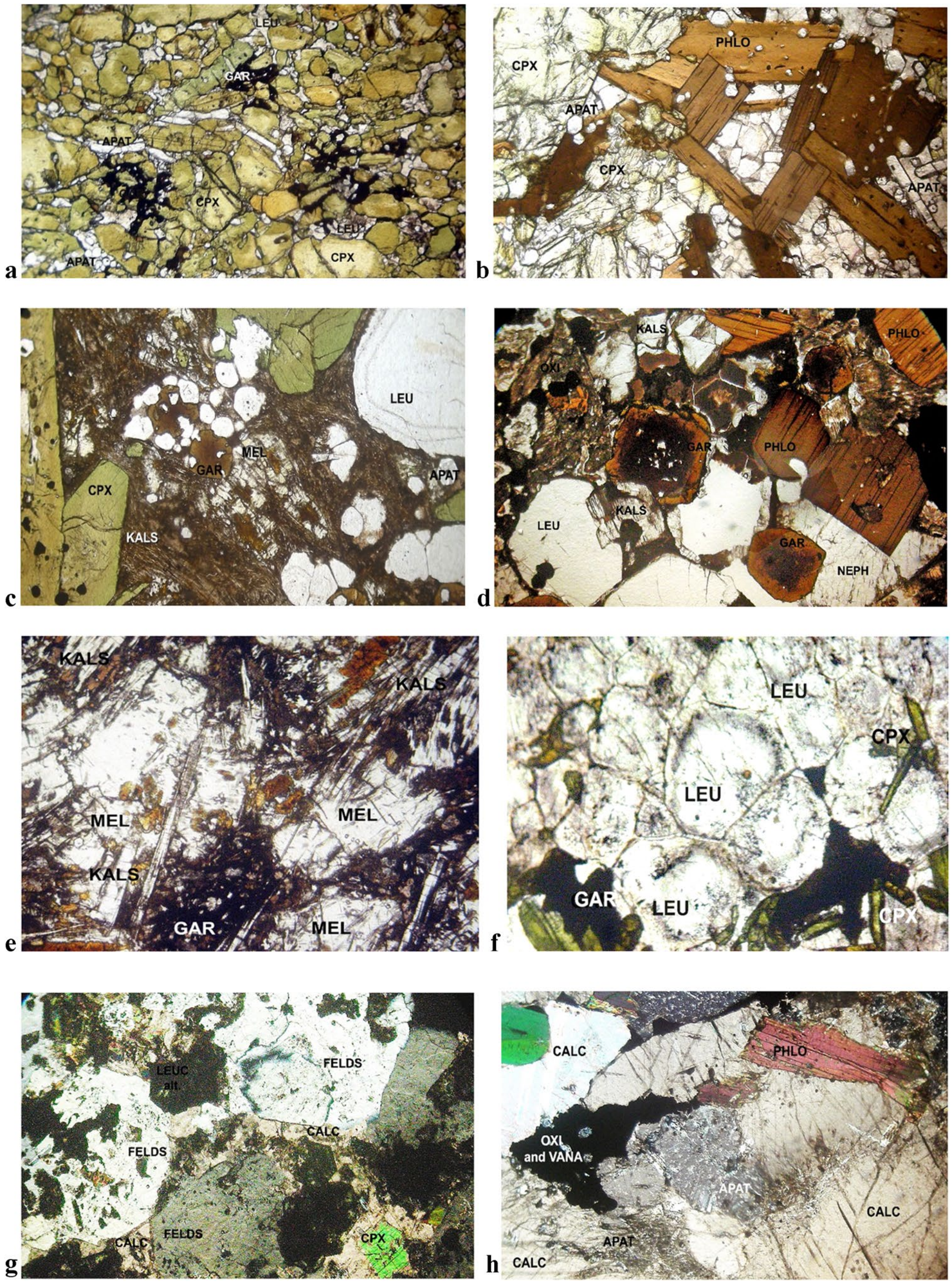

Fig. 2 Rock textures: **a** pyroxenite with clinopyroxene, apatite, and garnet; **b** pyroxenite with clinopyroxene, apatite, and phlogopite; **c** microgranular texture of kamafugite with clinopyroxene, apatite, leucite, melilite, and kalsilite; **d** coarse-grained texture of kamafugite with clinopyroxene, apatite, leucite, garnet, kalsilite, and phlogopite; **e** melilitite with melilite, apatite, kalsilite, and garnet; **f** leucitolite with leucite, clinopyroxene, garnet (coarse-grained texture); **g** feldspar-bearing syenite with clinopyroxene, ghost of leucite, alkali feldspar, and calcite; **h** carbonatite with calcite, apatite, phlogopite, Fe-oxide, and vanadinite

Analytical methods

Mineral compositions were determined at CAMPARIS Lab. (Université Paris-Sorbonne, France), using the Cameca SX 100 or Cameca SX Five electron probe microanalyzers (with 4 or 5 wavelength-dispersive spectrometers). Element calibrations were done using a set of silicates, oxides, and REE-dopped glasses. Accelerating voltage and beam current were $U=15$ kV, $I=10$ nA, with a beam of 1–5 µm wide; the counting times for each element were 10 s and 5 s for background on each side of the measured X-ray peak for each element. The mineral compositions are calculated using a Z.A.F. iterative matrix correction. Mineral structural formulae were calculated on a classical stoichiometric basis chosen for each mineral species.

^{18}O and ^{13}C stable isotope analyses were carried out on calcite extracted from magmatic rocks and the limestone basement. Calcite powder was reacted with 100% orthophosphoric acid at 25 °C and the derived CO_2 was analyzed using a VG Sira 10 mass spectrometer to determine O and C isotope composition at the GEOPS laboratory (Université Paris-Saclay, France). All isotopic values are reported in the standard δ-notation in per mil relative to V-PDB (Vienna Pee Dee Belemnite) by assigning a δ^{13}C value of $+1.95‰$ and a δ^{18}O value of $-2.20‰$ to NBS19. Reproducibility was checked by a replicate analysis of laboratory standards and was $\pm 0.1‰$ for carbon isotopes and $\pm 0.2‰$ for oxygen isotopes.

Whole-rock major and trace element concentrations of the samples were determined by inductively coupled plasma optical emission spectrometry and inductively coupled plasma mass spectrometry, respectively at the Service d'Analyse des Roches et des Minéraux (SARM, CRPG, Nancy, France). CO_2 analyses of the fire loss on ignition were carried out for each rock.

The volcanoclastic deposit: leucitite and peperite

The volcanoclastic deposit consists of a brecciated and hydrothermally altered leucitite (Fig. 1e). At the base of the deposit, there is a 50-cm-thick layer of a mixture of dark leucitite granules enclosed in a white matrix composed essentially of calcite and zeolites. This 50-cm-thick layer seems to be a peperite (Fig. 1f). Similar deposits are commonly described during explosive phreatomagmatic eruptive events occurring within lacustrine areas. The gray-black leucitite granules contain phenocrysts of clinopyroxene and leucite in an essentially dark microlithic groundmass composed of opaque oxide, feldspar, clinopyroxene, apatite, and glass. The granules are surrounded by a matrix composed of calcite and zeolites. Some clinopyroxenes are isolated during the granulation process of leucitite. The volcanoclastic deposit also contains some well-preserved angular to more rounded enclaves of leucitite, very similar in texture and mineral paragenesis to the leucitite matrix of the volcanoclastic deposit.

Main petrological groups of xenoliths

Forty xenoliths were investigated and divided into five groups (Table 1), according to their mineral paragenesis (Table 1): pyroxenites, plutonic kamafugite-type rocks, leucitolites, syenites, and only one carbonatite xenolith.

The pyroxenite xenoliths

Pyroxenites (Fig. 2a, b; Table 1) are ultramafic rocks with more than 90 vol.% of mafic minerals (clinopyroxene, phlogopite) associated with numerous prismatic crystals of apatite and minor amounts of interstitial felsic minerals (< 10 vol.%). Phlogopite, when present (0–20 vol. %), is typically subhedral to anhedral, crystallizing after clinopyroxene and apatite (Fig. 2b). Dark interstitial melanite-type garnet, leucite, zeolites, and calcite are present in small amounts. Leucite is commonly replaced by a mixture of zeolite, calcite, and phyllosilicate. These xenoliths are very similar to ultramafic xenoliths from the Potassic Ultrapotassic Afyon volcanic Province described by Prelević et al. (2015).

The kamafugite-type xenoliths

These xenoliths contain from 5 to 30 vol.% of kalsilite ($KAlSiO_4$), 25–30 vol.% of leucite, nepheline, and no feldspar. Kalsilite has never been described before in the previous studies of the Potassic-Ultrapotassic Afyon volcanic Province (Akal et al. 2013; Prelević et al. 2015; Elitok 2019). It also occurs in the Western Africa Rift ultrapotassic magmatism and in the Italian Roman Province (Di Battistini et al. 2001; Tappe et al. 2003; Stoppa et al. 2003a). Two main textures of kamafugite-type xenolith are observed: a microgranular porphyritic texture and a coarse-grained texture.

The microgranular porphyritic xenoliths have variable modal compositions (Fig. 2c, Table 1) with porphyrocrysts of leucite, zoned clinopyroxene including tiny early Ti-magnetite, prismatic melilite, and later idiomorphic zoned (black core to yellow rim) garnet and magnetite. Kalsilite is typically the last major mineral to crystallize in these rocks, after apatite, clinopyroxene, magnetite, melilite, and just before garnet. Garnet includes other phases like melilite,

Table 1 Modal composition of studied plutonic xenoliths and leucitite

Rock Nb	98-A	98,004	98,006	98,005	98,008	E-17	E8	E9	E12
	Melilitolite		Kamafugite group			Carbonatite		Pyroxenite group	
Leucite		30	30	25	25		5	5	+
Melilite	45		10	15	7				
Kalsilite	30	5	15	25	15				
Nepheline		18	5		20				
Altered foide		5	10		5				
Feldspath					+				
Clinopyroxene				20	15		80	60	75
Garnet	20	15	10	10			5		
Calcite		3	10		3	90		2	5
Apatite	2	2	3		+	5	8	7	7
Mica		18			10	2		25	
Titanomagnetite		+		5	+	2			
Others (zeolites)	3	+	5		+	1	2	1	12
Groundmass									

Rock Nb	E11	E3	E4	E5	E6	E7	E10	E2
	Leucititolite group						Syenite	Leucitite
Leucite	70	45	65	70	60	60	10	30
Melilite								
Kalsilite		3				3		
Nepheline								
Altered foide	5	7			10	10	5	+
Feldspath			3				65	+
Clinopyroxene	10	35	20	10		5	5	20
Garnet	10		10	15	12	10		
Calcite					5		10	
Apatite		5	2	2	2	3	2	+
Mica	5		2	2	5		2	
Titanomagnetite								+
Others (zeolites)		3					1	+
Groundmass								50

apatite, and thin elongate prisms of kalsilite, attesting of its late nucleation and growth. Kalsilite exhibit clusters of very elongated homogeneous prisms forming the micro-granular groundmass of the rock (Fig. 2c).

The coarse-grained xenoliths (Fig. 2d, e) not only have the same mineralogy, with apatite, leucite, prismatic kalsilite, and zoned garnet but they also contain phlogopite. Clinopyroxene is less abundant and melilite is rare or absent. In coarse-grained xenoliths, kalsilite and nepheline crystallize as separate phases. Kalsilite forms euhedral, tabular crystals (Fig. 2d) showing kalsilite-nepheline exsolution intergrowths (Fig. 3), symptomatic of subsolidus reequilibration. Such exsolution intergrowths have been described in Mt Nyiragongo lava (Congo), in melilitolites, kalsilitites, and kamafugites from Roman Province and Intramountain Ultra-alkaline Province, Italy (Aurisicchio and Federico 1985; Federico et al. 1994; Stoppa et al. 2003a). Melilite is associated with variable amounts of clinopyroxene, garnet, apatite, phlogopite, Ti-magnetite, and calcite, while olivine is not present. Calcite and brown-yellowish phases (a mixt of hydroxide amorphous phases and phyllosilicates) commonly replace the core of melilite crystals. Intergrowth features between garnet and leucite are common. Large crystals of nepheline can be relatively abundant (5 to 20 vol.%) in these xenoliths and calcite is interstitial. Two small (no more than 5 cm in size) mafic–ultramafic xenoliths also belong to this group. The first xenolith is extremely rich in melilite (45 vol.%, Table 1 sample 98-A), and can be named melilitolite. The second xenolith is a garnet-rich type; a similar garnet-bearing xenolith has been also described in the leucitites from the Balç1khisar volcanic area (Akal et al. 2013).

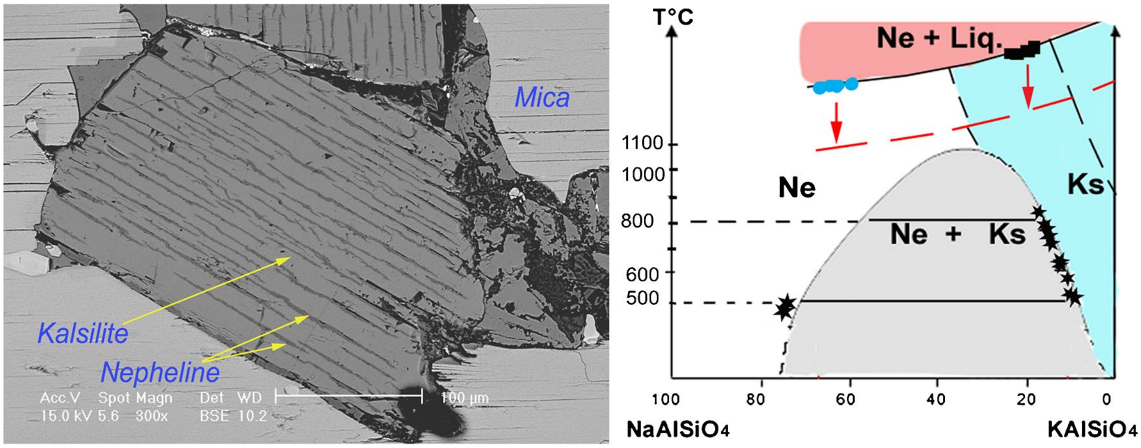

Fig. 3 Kalsilite and nepheline compositions. Microprobe backscattered picture of euhedral kalsilite, crystal showing exsolutions features: fine exsolutions lamellas of nepheline. Nepheline-kalsilite versus T°C diagram showing the position of kalsilite analyses in relation with solidus and solvus curves; the red curve is a more realistic solidus position relative to temperature for the hypersolvus kalsilite. The blue line would be the solidus-solvus intersection given by the compositions of separate crystals of nepheline and exsolved kalsilite found in coarse-grained kamafugite-type xenolith (after Tuttle and Smith 1958; Zeng and MacKenzie 1984)

The leucitolite xenoliths

Leucitolites are the commonest and largest plutonic xenoliths (10–15 cm in size). They are mostly coarse-grained and their mineral parageneses differ only in the relative mafic to felsic mineral ratio, in particular leucite, varying from 45 to 70 vol.%, and giving mesocratic to leucocratic type rocks (Fig. 2f). Adjacent crystals of leucite typically show 180° triple joins, suggesting leucite crystal segregation, followed by textural subsolidus re-equilibration and crystal aging (Boudreau 1995; Marsh 1998, 2007; Laporte and Provost 2000; McBirney 2007; McBirney et al. 2009). This process of subsolidus re-equilibration can happen during slow cooling of magmatic intrusions, but it remains controversial in particular for felsic intrusions (Holness and Vernon 2014; Holness et al. 2017, 2018). Leucite is locally partially replaced by a mixture of alkali feldspar and zeolite. The other mineral phases are euhedral green clinopyroxene, prismatic apatite, poikilitic garnet, Ti-Fe oxides, and phlogopite. Kalsilite is rare in leucitolite and occurs as poikilitic, commonly altered crystals located between euhedral leucite crystals. Textural features such as two-phase layering, with pyroxene-rich thin layers and extremely rich leucite layers, are symptomatic of crystal segregation by a rheological process or by a density-driven cumulative process within the magma intrusions.

Feldspar- and leucite-bearing syenite xenoliths

Their textures are fine-grained to coarse-grained (Fig. 2g). As for kamafugite-types and leucitolites, the mineral paragenesis consists of not only euhedral zoned (green core to dark green rim) clinopyroxene, prismatic apatite, and euhedral leucite but also rare euhedral kalsilite prism in some xenoliths, and sometimes nepheline. Zoned garnet and poikilitic zoned alkali feldspar are observed. Few sections of pale-brown mica and Ti-Fe oxides are observed. The paragenesis variations from one sample to one another are dependent upon the destabilization degree of leucite which is partially or totally replaced by large, poikilitic feldspars. Calcite also crystallized as a primary phase in some feldspar-bearing syenite, in relation to a CO_2-enriched dissolved fluid phase.

The carbonatite xenolith

A single 10-cm-sized xenolith of carbonatite has been found, representing the first occurrence of coarse-grained carbonatite in this area. It consists of large crystals of calcite with clusters of prismatic apatite. Frequent pale-brown phlogopite exhibits sector zoned subhedral crystals. Magnetite and vanadinite have crystallized lately and are interstitial between calcite and apatite crystals (Fig. 2h).

At the apex of the so-called Isparta Angle, from the Senirkent area (Elitok 2019), inclusions and microscopic blobs of carbonatite have been also observed in a leucite-bearing phonolite. These small blobs and inclusions are mainly formed by carbonate with various amounts of phlogopite, clinopyroxene, leucite or nepheline, apatite, and garnet (Elitok 2019).

Mineral composition results

Leucite

Leucite compositions (Appendix 1A) are usually near the ideal formulae with very small amounts of Na_2O, FeO, and

BaO (< 0.8 wt.%). The leucite of pyroxenite and syenite has undergone hydration. It has been partially replaced by a mixture of feldspar, calcic zeolite, and calcite (see altered leucite in Appendix 1A). Replacement of leucite by analcite is not observed, probably due to very low sodium content. The main feature that occurs in some syenite xenoliths is the partial or almost total disappearance of leucite, replaced by alkali feldspar and nepheline, corresponding to the subsolidus breakdown of leucite in the presence of water (Fudali 1963).

Kalsilite and nepheline

Homogeneous thin elongate prisms of kalsilite (Fig. 3; Appendix 1B) are relatively Na_2O-rich with a maximum of 21 mol% of nepheline, corresponding to the preserved hypersolvus composition of kalsilite during rapid cooling. Based on the experimental study of Tuttle and Smith (1958), the crystallization temperature would be ≥ 1000 °C (Fig. 3).

The kalsilite of the coarse-grained kamafugite-type contains 7–11 mol% of nepheline component, and the exsolved nepheline lamellae have 25–26 mol% of kalsilite component, indicating a solvus exsolution process during slow cooling, operating between 800 and 500 °C. In coarse-grained kamafugite and feldspar-bearing syenite, crystals of nepheline rim leucite form large anhedral crystals showing some cancrinite-type alteration. Compared to the nepheline exsolution lamellae from the exsolved kalsilite crystals, these nepheline crystals are relatively potassic, with 35–39 mol% of kalsilite component. This compositional range (Fig. 3) is consistent with the subsolvus kalsilite-nepheline pairs crystallizing as separate crystals, at about 800 °C under 0.5 GPa, according to the experimental study of Zeng and MacKenzie (1984), whereas the solvus exsolution process of kalsilite has operated between 800 and 500 °C during slow cooling (Fig. 3).

Alkali feldspar

The first feldspar to crystallize in syenite belongs to the hyalophane type (Appendix 1C). Crystals are strongly zoned; the Ba-rich core has 12–13 wt.% BaO, giving 25 mol% of celsian component, and subsequent decrease of K_2O and Na_2O wt.%. SrO reaches a maximum of 2.5 wt.% corresponding to 6 mol.% of the stronalsite component $Na_2SrAl_4Si_4O_{16}$ (see Essene et al 2005). Crystal rims evolve to pure K-feldspar. The feldspar of the leucitite lava is also Ba-rich (25 mol% of celsian component) and is more Ca- and Sr-rich than those of the syenite. This Ba-feldspar is plotted in the quartz-nepheline-kalsilite ternary system (Fig. 4). Ba, equivalent of K and Na, is allocated to the calculated nepheline and kalsilite components. The hyalophane feldspar plots in the feldspathoid-bearing area of that diagram, due to Ba enrichment and coupled Si-Al substitution. When leucite was replaced during the crystallization of silica-undersaturated, Ba-rich, K-rich, and Na-poor magma, hyalophane feldspar crystallized in place of kalsilite or nepheline, which are both unable to incorporate large amounts of Ba and Sr in their

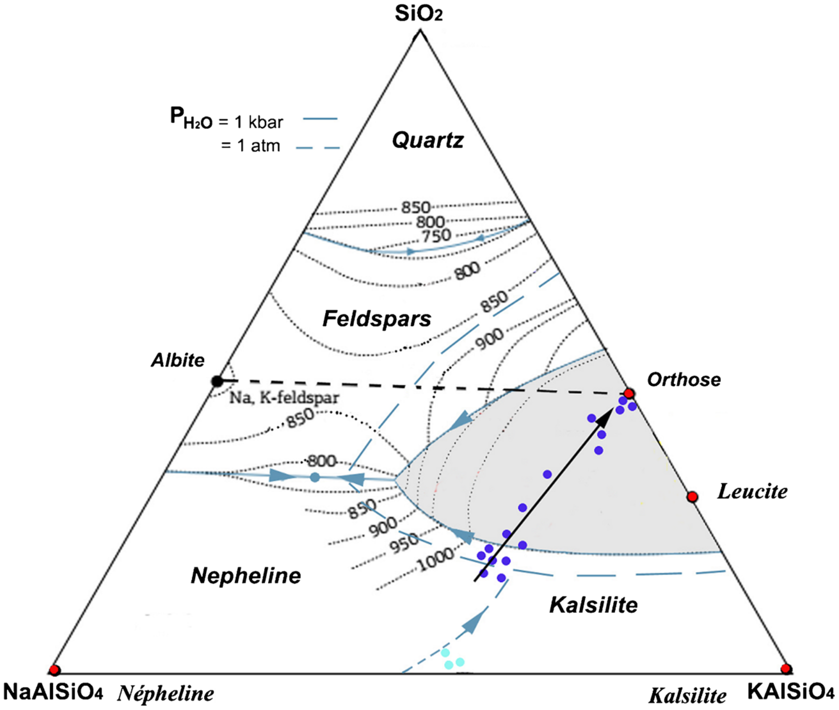

Fig. 4 Hyalophane and K-feldspar in the system nepheline-kalsilite-quartz ternary diagram. Considering that Sr and Ba are equivalent to Na and K with equal repartition between the two poles. Blue dots: present study; pale-blue dots: analyses from Akal (2003)

structures. In the Qz-Ne-Ks diagram, hyalophane feldspar plays the same role as feldspathoid because of its strong silica deficiency compared to typical K-feldspar. The E10 feldspar-bearing syenite (Table 2) illustrates this well: the rock is strongly silica-deficient, Ba- and Sr-rich (11,000 ppm of Ba, 2250 ppm of Sr), and Na-poor (0.25w.% Na_2O). Leucite was destabilized and was first replaced by hyalophane feldspar instead of kalsilite or/and nepheline, followed by K-feldspar crystallization. The control by Sr and Ba on feldspar crystallization has been previously pointed out by Ferguson and Cundari (1982) in leucite-bearing magmas. Ba and Sr elements are important substitutes for K, Na, and Ca, particularly in potassic-ultrapotassic silica-undersaturated magmatism (Cundari 1979; Mitchell and Vladikin 1996; Akal 2003; Platevoet et al. 2014; Caran 2016). To the best of our knowledge, there seems to be no experimental system that investigates the effect of Ba and Sr on the stability of feldspar-feldspathoid phases in the Qz-Ne-Ks ternary system, and also in the more complex Qz-Ne-Ks-An quaternary system (Carmichael et al. 1974). These systems would probably show major changes if Ba and Sr elements were considered instead of Na, in a K-rich, highly silica-deficient experimental system.

Clinopyroxene

The composition of clinopyroxene (Appendix 1D) evolves from diopside to augite and from augite to aegirine-augite in the most evolved rocks. CaO and MgO contents are high, especially in crystal cores of ultramafic and mafic xenoliths (Fig. 5), but decrease from kamafugite-type to leucitolite, syenite xenolith, and in leucitite lava. CaO and MgO contents decrease in the crystal rims together with SiO_2, while FeOt, Al_2O_3 (<4.60 wt.%), and TiO_2 (<1.4 wt.%) contents increase, probably due to the decrease of silica activity during the crystallization. The aegirine component rises in the more evolved syenite xenoliths and in leucitite, a common feature of the silica-undersaturated series evolving under relative oxidizing conditions, and/or due to the alkali-ferric effect in peralkaline magmas (Larsen 1976; Mitchell and Platt 1978, 1982; Mitchell and Vladykin 1996). Tschermak molecules, especially Fe-Tschermak mol., rise from core to rim of crystals and from the less evolved ultramafic–mafic groups (pyroxenite and kamafugite) to the more felsic groups (leucitolite and syenite) and leucitite. In the Ti vs. Al_t diagram (Fig. 5), the majority of clinopyroxene analyses plot in the transitional field and the HKS-KS field of Perini and Conticelli (2002) and in the kamafugite field for pyroxene depicted by Prelević et al. (2005, 2015). However, some analyses of the kamafugite xenoliths are very poor in TiO_2. This can be due to early crystallization of both Ti-magnetite and clinopyroxene (rock 98005, Fig. 2c), Ti being prior incorporated in Ti-magnetite under relative elevated fO_2. The clinopyroxene of melilite leucitite from Meşebaşi described by Akal (2003) belongs to the lamproite field of Mitchell and Bergman (1991) and differs from clinopyroxene of the Eğirdir leucitite lava.

Melilite

Compositions of melilite (Appendix 1E) are plotted in the Na-melilite/gehlenite/akermanite ternary system (Fig. 6). They are poor in gehlenite and rich in akermanite components. They are relatively similar in composition to melilite from Montefiascone pyroxenites of the Roman Province and San Venanzo melilitolite (Stoppa et al. 2003a), but they are lower in gehlenite than the melilites of the Alban Hills ejecta (Stoppa et al. 2003a). Finally, they are more Mg-rich, and Al- and Na-poor compared to the melilite of the northern Meşebaşi melilite-bearing leucitites from the northern Potassic-Ultrapotassic Afyon volcanic Province (Akal 2003).

Phlogopite

All mica can be classified as phlogopite (Appendix 1F) with a Mg/Mg + Fe + Mn ratio ranging from 0.90 to 0.60. Their Ti content is highly variable, being generally > 2.5 wt.% in pyroxenite and decreasing through kamafugite and leucitolite groups, and is very low in phlogopite from syenite and carbonatite xenoliths. F content is low to moderate in pyroxenite, leucitolite, and kamafugite-type (from 0.3 to 1.13 cation pfu.), but more elevated in the feldspar-bearing syenite with 1.2 to 2.6 cations pfu., probably in relation with a [F + CO_2]-rich, H_2O-poor dissolved fluid phase. BaO in phlogopite is high and increases from pyroxenite to kamafugite and leucitolite, from around 1.0 up to 6.1 wt.%. The main coupled substitution that governs Ba incorporation involves Si, Al, and Ti, also Fe and Mg, in place of Ti and K in the interlayer site (Wagner and Velde 1986; Wagner et al. 1987; Edgar 1992; Seifert and Kämpf 1994). The most barium-rich phlogopite occurs in the carbonatite xenolith with a maximum of 13 wt.% BaO. The crystals show obvious sector zoning (Fig. 7A) due to strong Ba variations associated with coupled Al, Si, and K substitutions. The correlation (Fig. 7B) observed between [Ba + Al_{IV}] and [Si + K] pointed out the main substitution:

$$Ba^{2+} + Al^{3+} = K^{+} + Si^{4+}$$

Ba-rich phlogopite is frequent in potassic-ultrapotassic magmatism. Such high BaO values, between 13 and 16 wt.%, have been observed in phlogopite (Fig. 7C) from the Jacupiranga carbonatite, Brazil (Gaspar and Wyllie 1982), and also in phlogopite of numerous nephelinites,

Table 2 Major and trace elements whole-rock analyses, and calculated CIPW norm

Whole-rock	Kamafugite-type rocks			Syenite	Leucitites		Pyroxenites			Leucitolites						Carbonatite
analysis	Melilitolite	Kalsilite rock	Kalsilite rock			* Most altered	Phlo. Leuc									
rock Nb	98,005	98–004	98–008	E10	E2	E1*	E9	E12	E8	E3	E4	E7	E5	E11	E6	E17
SiO2	41.21	35.54	36.50	44.59	49.89	43.65	41.35	42.06	45.24	48.04	45.14	45.93	48.29	45.42	45.30	0.75
TiO2	1.42	2.63	2.13	0.79	0.85	1.36	0.86	0.69	0.81	0.53	0.95	1.57	0.72	3.19	0.79	0.12
Al2O3	13.64	11.97	13.68	14.03	15.69	12.34	5.56	3.08	6.45	14.43	14.70	15.06	15.98	16.76	17.20	0.40
Fe2O3	9.29	10.93	12.10	5.47	6.77	8.34	4.53	5.06	5.44	4.07	10.59	9.27	5.23	6.71	4.98	4.17
MnO	0.15	0.17	0.19	0.10	0.13	0.10	0.07	0.07	0.08	0.05	0.10	0.12	0.08	0.05	0.10	0.14
MgO	2.92	5.09	3.17	2.48	3.41	4.90	14.63	11.70	10.60	4.85	3.76	2.82	3.92	0.58	2.40	0.50
CaO	16.11	16.21	13.64	13.92	8.67	15.52	21.23	29.41	23.32	12.79	9.58	9.44	9.12	9.95	8.00	51.35
Na2O	1.17	0.40	1.14	0.25	1.48	0.16	0.13	0.13	0.22	0.18	0.17	0.39	0.25	0.19	1.04	0.02
K2O	8.56	7.21	8.57	9.17	8.00	4.43	3.24	0.29	2.77	9.49	9.39	10.85	11.57	12.01	12.75	0.10
P2O5	0.80	0.88	0.48	0.53	0.65	0.90	4.80	5.89	3.78	1.39	0.68	0.48	0.72	0.18	0.47	2.58
Pf (F+H20)	3.64	3.07	3.25	1.36	3.19	7.67	1.44	1.06	1.85	3.32	4.48	3.11	3.61	4.36	2.78	0.37
CO2	2.07	4.71	3.85	5.98	0.10	0.18	1.12	1.26	0.19	0.46	0.05	0.12	0.27	0.10	3.17	37.99
Total	100.98	98.81	98.70	98.65	98.82	99.56	98.95	100.70	100.75	99.60	99.58	99.18	99.77	99.49	98.96	98.48
ppm																
As	3.87	2.21	3.19	15.69	3.05	<L.D	<L.D	1.23	1.27	<L.D	<L.D	1.96	<L.D	<L.D	1.33	35.79
Ba	1766.00	6945.00	6729.00	11,070.00	4515.00	2253.00	2506.00	360.30	1423.00	1826.00	2289.00	3761.00	3051.00	2048.00	5060.00	4160.00
Be	13.64	5.67	4.24	10.02	9.47	4.60	2.58	1.85	3.09	2.20	3.76	9.48	6.04	1.49	5.35	<L.D
Bi	0.66	0.43	0.15	<L.D	<L.D	0.13	<L.D	<L.D	<L.D	<L.D	<L.D	0.47	<L.D	0.15	<L.D	8.48
Cd	0.37	0.79	0.66	0.40	0.28	0.32	0.12	0.14	0.10	<L.D	0.13	0.43	0.17	0.93	0.24	0.70
Ce	180.60	213.70	319.50	130.00	154.00	109.50	125.70	393.90	173.70	96.18	61.52	92.55	76.09	82.90	94.22	881.20
Co	29.55	32.94	28.07	10.78	16.85	28.48	34.67	30.46	30.47	17.55	33.28	24.30	18.02	6.87	15.32	3.60
Cr	72.22	59.30	<L.D	44.52	39.35	10.13	1566.00	413.50	574.60	17.69	6.50	4.44	9.59	<L.D	12.63	<L.D
Cs	20.17	15.67	13.74	5.67	24.64	5.31	5.01	0.78	9.86	34.83	20.43	49.67	27.97	31.58	56.74	0.09
Cu	189.30	211.60	156.70	55.19	42.58	61.54	7.74	12.25	27.41	7.96	12.96	73.74	32.44	67.35	40.74	<L.D
Dy	5.23	15.67	7.57	4.67	4.69	4.76	4.26	8.82	4.39	2.16	1.78	6.73	2.10	19.10	2.45	1.26
Er	1.98	7.15	3.35	2.11	2.09	1.95	1.31	2.66	1.42	0.70	0.65	2.94	0.77	8.73	1.01	0.41
Eu	4.03	7.50	4.82	2.57	2.60	2.91	3.42	8.03	3.51	1.77	1.23	3.48	1.38	8.50	1.63	1.40
Ga	20.84	19.72	22.04	21.71	17.77	11.46	8.05	8.15	9.17	11.66	14.04	17.28	14.23	15.18	18.03	6.28
Gd	10.24	22.44	12.44	7.49	7.35	8.12	9.59	20.83	9.56	4.75	3.42	10.14	3.89	25.62	4.43	3.62
Ge	1.35	2.16	1.98	1.29	1.37	1.46	1.66	2.15	1.86	1.07	1.05	1.34	1.10	1.98	0.97	0.41
Hf	8.00	34.28	18.46	12.46	10.19	14.18	3.00	7.12	6.65	4.79	4.60	18.27	5.76	51.16	7.88	0.12

Table 2 (continued)

Whole-rock	Kamafugite-type rocks			Syenite	Leucitites		Pyroxenites			Leucitolites						Carbonatite
Ho	0.79	2.72	1.23	0.78	0.79	0.76	0.59	1.22	0.62	0.31	0.27	1.14	0.32	3.38	0.38	0.13
In	< L.D	0.11	0.11	< L.D	< L.D	0.09	< L.D	0.07	< L.D	< L.D	< L.D	0.07	< L.D	0.10	< L.D	< L.D
La	84.84	94.96	135.90	70.09	81.02	45.48	57.25	202.40	88.64	47.69	30.25	41.66	37.17	18.87	48.99	662.00
Lu	0.25	0.91	0.50	0.30	0.28	0.24	0.12	0.21	0.14	0.07	0.08	0.38	0.09	1.07	0.15	0.03
Mo	0.74	0.81	2.16	13.32	0.71	< L.D	< L.D	< L.D	< L.D	< L.D	0.63	< L.D	1.13	0.56	0.61	1.38
Nb	22.24	23.74	100.60	25.16	24.51	7.41	3.33	1.06	1.28	0.58	3.46	12.63	7.72	14.51	12.49	83.65
Nd	96.17	125.80	145.90	63.26	62.62	59.72	78.44	203.50	87.05	48.25	30.47	56.51	35.84	95.31	43.15	138.50
Ni	22.02	27.62	10.08	16.05	22.29	24.57	135.10	71.76	73.58	19.93	21.71	8.20	16.84	4.50	11.02	4.52
Pb	103.03	63.00	34.19	243.43	76.05	12.46	2.40	4.26	5.18	2.15	5.01	61.31	15.04	14.07	18.29	1618.68
Pr	23.11	27.91	38.10	15.74	17.29	13.05	17.83	48.47	21.28	11.65	7.40	12.29	9.15	15.95	10.95	62.68
Rb	363.20	345.30	275.80	238.60	962.50	386.90	202.90	30.34	232.00	836.70	873.70	749.20	721.80	800.40	850.10	3.93
Sc	< L.D	22.46	< L.D	< L.D	12.72	23.93	36.23	63.78	44.69	23.35	21.45	13.86	18.93	24.19	< L.D	< L.D
Sb	0.41	0.17	0.31	1.90	0.40	< L.D	< L.D	< L.D	< L.D	< L.D	< L.D	0.11	< L.D	< L.D	0.20	0.30
Sm	17.78	29.06	22.25	11.66	10.82	11.82	15.24	34.76	15.17	7.81	5.36	13.10	6.08	30.13	7.32	8.24
Sn	4.91	13.05	7.62	4.26	4.19	7.45	1.26	3.50	4.60	2.84	3.50	8.25	2.96	20.36	3.23	0.45
Sr	1626.00	740.20	423.60	2256.00	3592.00	1508.00	778.10	1517.00	1325.00	581.30	514.80	811.00	978.80	471.40	1046.00	11,960.00
Ta	2.66	3.61	8.09	1.61	1.83	1.03	0.34	0.37	0.36	0.06	0.33	1.24	0.68	3.19	1.11	0.04
Tb	1.19	3.05	1.59	0.94	0.95	1.00	1.01	2.18	1.03	0.52	0.40	1.33	0.46	3.60	0.53	0.37
Th	39.49	48.75	74.22	41.76	41.92	20.49	10.12	36.11	16.35	11.78	10.91	22.59	15.63	22.03	22.43	0.10
Tm	0.26	1.00	0.48	0.30	0.30	0.26	0.15	0.28	0.16	0.08	0.08	0.41	0.10	1.19	0.14	0.04
U	8.22	11.27	20.10	18.53	6.88	3.94	1.68	2.64	1.59	1.16	1.71	6.73	3.70	7.23	8.85	7.81
V	239.20	332.90	522.50	214.40	152.50	140.80	65.70	78.96	92.63	52.80	127.50	207.60	79.04	175.40	155.50	331.50
W	1.16	0.88	1.55	25.35	0.76	< L.D	< L.D	0.12	< L.D	< L.D	0.13	0.21	0.16	0.21	0.14	0.30
Y	24.41	78.22	40.02	25.43	25.59	22.03	17.03	34.24	18.23	8.54	7.80	31.97	9.11	90.88	12.22	3.91
Yb	1.65	6.40	3.29	2.00	1.93	1.65	0.83	1.55	0.94	0.48	0.52	2.63	0.61	7.44	0.93	0.22
Zn	118.90	108.70	43.73	59.34	80.97	47.61	41.12	27.94	34.76	19.09	58.40	87.97	37.84	26.25	59.29	41.58
Zr	495.30	1307.00	1000.00	609.00	414.40	463.10	97.79	163.00	172.20	104.10	132.70	580.40	177.80	1524.00	341.70	9.04
CIPW norm																
Quartz	0.00	0.00	0.00	0.00	0.00	0.00	0.00	0.00	0.00	0.00	0.00	0.00	0.00	0.00	0.00	
Plagioclase	5.96	6.74	4.18	5.58	11.63	18.96	4.00	7.85	6.82	9.81	10.67	6.50	7.07	8.57	2.57	
Orthoclase	0.00	0.00	0.00	17.92	36.24	4.68	0.00	0.00	0.00	2.54	0.00	0.00	0.00	0.00	1.63	
Nepheline	5.36	1.83	5.23	1.15	6.78	0.73	0.60	1.01	0.60	0.83	0.78	1.79	1.15	0.87	4.77	
Leucite	40.80	37.85	41.80	35.50	10.08	18.29	16.61	13.75	1.57	43.13	44.99	51.53	55.55	56.96	60.99	
Kalsilite	0.00	0.00	1.58	0.00	0.00	0.00	0.00	0.00	0.00	0.00	0.00	0.00	0.00	0.00	0.00	

Table 2 (continued)

Whole-rock	Kamafu-gite-type rocks			Syenite	Leucitites		Pyroxen-ites			Leucito-lites						Carbonatite
Corundum	0.00	0.00	0.00	0.00	0.00	0.00	0.00	0.00	0.00	0.00	0.00	0.00	0.00	0.00	0.00	
Diopside	13.94	3.54	0.00	18.87	22.15	40.58	41.77	58.32	66.93	33.45	25.60	22.92	24.83	7.98	11.75	
Hypersthene	0.00	0.00	0.00	0.00	0.00	0.00	0.00	0.00	0.00	0.00	0.00	0.00	0.00	0.00	0.00	
Wollastonite	0.00	0.00	0.00	0.00	0.00	0.71	0.00	0.00	0.00	0.03	0.00	0.00	0.00	9.62	0.00	
Olivine	6.66	14.27	13.90	1.53	3.13	0.00	14.59	2.75	1.67	0.00	5.53	2.92	1.98	0.00	3.54	
Larnite	12.20	10.54	11.19	0.00	0.00	0.00	3.10	2.73	2.16	0.00	0.45	2.84	0.44	2.05	0.00	
Acmite	0.00	0.00	0.00	0.00	0.00	0.00	0.00	0.00	0.00	0.00	0.00	0.00	0.00	0.00	0.00	
K2SiO3	0.00	0.00	0.00	0.00	0.00	0.00	0.00	0.00	0.00	0.00	0.00	0.00	0.00	0.00	0.00	
Na2SiO3	0.00	0.00	0.00	0.00	0.00	0.00	0.00	0.00	0.00	0.00	0.00	0.00	0.00	0.00	0.00	
Rutile	0.00	0.00	0.00	0.00	0.00	0.00	0.00	0.00	0.00	0.00	0.00	0.00	0.00	0.00	0.00	
Ilmenite	2.70	4.99	4.05	1.50	1.61	2.58	1.63	1.54	1.31	1.01	1.80	2.98	1.37	6.06	1.50	
Magnetite	2.70	3.18	3.51	1.58	1.96	2.42	1.32	1.58	1.46	1.17	3.07	2.68	1.52	1.94	1.45	
Hematite	0.00	0.00	0.00	0.00	0.00	0.00	0.00	0.00	0.00	0.00	0.00	0.00	0.00	0.00	0.00	
Apatite	1.85	2.04	1.11	1.23	1.51	2.09	11.12	8.76	13.65	3.22	1.58	1.11	1.67	0.42	1.09	
Zircon	0.10	0.27	0.21	0.12	0.27	0.27	0.27	0.03	0.03	0.01	0.03	0.12	0.03	0.31	0.07	
Perovskite	0.00	0.00	0.00	0.00	0.00	0.00	0.00	0.00	0.00	0.00	0.00	0.00	0.00	0.00	0.00	
Chromite	0.01	0.01	0.00	0.01	0.00	0.00	0.34	0.12	0.09	0.00	0.00	0.00	0.00	0.00	0.00	
Calcite	4.71	10.71	8.76	13.60	0.23	0.41	2.55	0.43	2.87	1.05	0.11	0.27	0.61	0.23	7.21	
Total	96.99	95.97	95.52	98.59	95.59	91.72	97.90	98.87	99.16	96.25	94.61	95.66	96.22	95.01	96.57	
Fe3+/(Fe3+Fe2)	20.0	20.0	20.0	19.9	20.0	20.0	20.1	20.0	20.0	19.9	20.0	20.0	20.1	20.0	20.1	
Mg/(Mg+Fet)	38.4	48.0	34.2	47.3	50.0	53.8	86.5	79.4	82.1	70.3	41.3	37.6	59.8	14.6	48.8	
DI	52.12	46.4	52.8	60.2	64.7	42.7	21.2	22.6	9.0	56.3	56.4	59.8	63.8	66.4	70.0	
agpa. Index	0.82	0.71	0.82	0.74	0.71	0.41	0.67	0.17	0.52	0.73	0.71	0.82	0.81	0.80	0.90	

*E1**, hydrothermalized leucitite matrix of the phreato-magmatic deposit; *DI*, differentiation index of Thornton and Tuttle (1960); *agpa. Index*, index of agpaicity

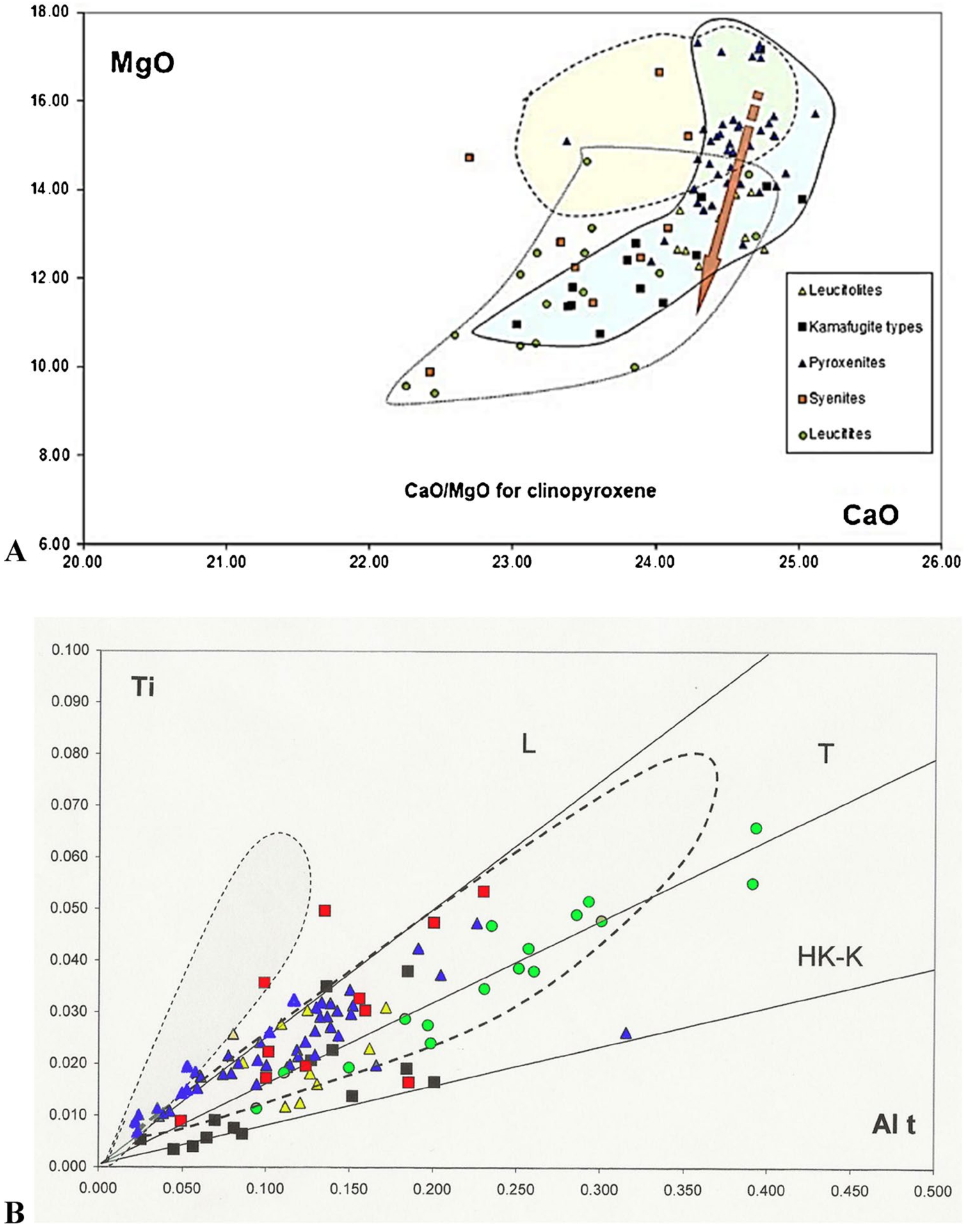

Fig. 5 **A** MgO versus CaO diagram (wt. %) for clinopyroxene. Arrow, evolution trend in pyroxenite xenoliths: the dotted fencing yellow field is for kamafugite from Prelević et al. (2005); the two other fields are for pyroxenite, kamafugite-type and leucitolites of the present study and leucitites of the present study. **B** Ti/Alt (a.p.f.u.) diagrams for clinopyroxene. L, lamproitic field after Mitchell and Bergman (1991); T and HK-K, transitional high-K and K series of Italian volcanic magmatism (after Perini and Conticelli 2002). Dotted fields: Cpx respectively from lamproites and kamafugites after Prelević et al. (2005)

ankaratrites, and kamafugites from various localities (Mansker et al. 1979; Gaspar and Wyllie 1982; Edgar 1992; Seifer and Kämp 1994; Stoppa et al. 2003c; Prelević et al. 2005; Caran 2016). Ba and Al-Si coupled substitution occurred exclusively in phlogopite when it crystallized before feldspar under high P_{H2O}, and in strongly silica-deficient magmas, prohibiting feldspar crystallization. It is also favored by a relatively high fO_2 and P_{H2O} (Edgar and Arima 1981). This is true for kamafugite, nephelinite, ankaratrite, and carbonatite. On the other hand, when alkali feldspar crystallizes, as it is in the feldspar-bearing syenite of the present study, Ba is preferentially incorporated into hyalophane and phlogopite remains Ba-poor.

Garnet

Garnet is strongly zoned from black core to brown-yellowish rim. Andradite (81–87%) and almandine (5–15 wt.%) are its main components (Appendix 1G). Black crystal cores are composed of melanite with > 15 wt.% TiO_2. Yellowish rims are Ti depleted and more Fe- and Ca-enriched with the increase of Fe-andradite and almandine components. MgO remains very low (< 1.3 wt.%) and decreases from garnet of kamafugite to those of syenite xenoliths. Melanite appears to be a systematic phase in the Potassic-Ultrapotassic Afyon Province magmatism and has been also described in melilite leucitites, melanite-bearing xenoliths from the Balç1khisar

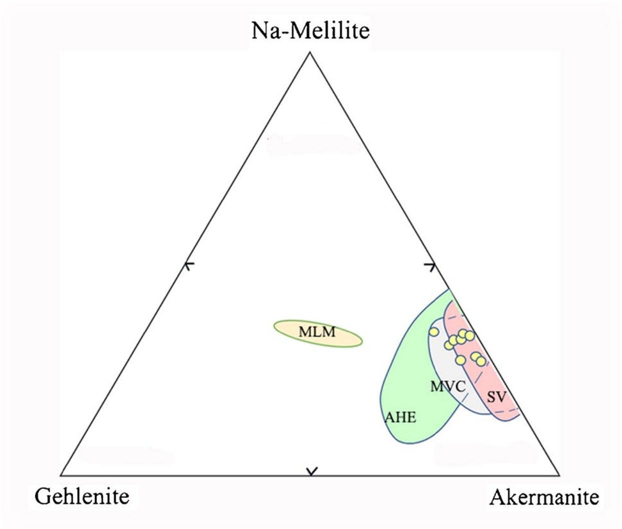

Fig. 6 Melilite compositions in the gehlenite–akermanite–Na melilite ternary diagram. Yellow dots, present study; SV field, San Venanzo volcanics, Intra-mountain Ultra-alkaline Province, Italy; AHE field, Alban Hill Ejecta, Roman Province, Italy; MVC, Montefiascone clinopyroxenite xenoliths, Roman Province, Italy; MLM, melilite-bearing leucitite, Meşebaşi area, Afyon K-UK Province Anatolia (after Stoppa et al. 2003a, b, c; Akal 2003)

area (Akal 2003; Akal et al. 2013), and in other localities of the western Taurides ultrapotassic volcanism (Prelević et al. 2015). Garnet is also present in leucitite and carbonatite inclusions from the Senirkent area of the Isparta Angle (Elitok 2019). Melanite has also been observed in other Ultrapotassic Provinces, such as in xenoliths of the Alban Hills ultrapotassic ejecta, Roman Province, Italy (Federico et al. 1994).

Other minerals

Apatite is observed in all xenolith groups and in leucitite. The composition variations (Appendix 2A, B) concern only SrO which varies between 0.3 and 1.2 wt.% but reaches up to 6.5 wt.% in the syenite. Silica is in the range 0.6–1.9 wt.%, but reaches 2.8 wt% in the apatite of carbonatite. F is relatively abundant with 1.5 to 2.4 wt.%, reaching 3.2–3.8 wt.% in the apatite of the syenite and leucitite. Apatite also contains REE, particularly the apatite of the carbonatite, with 1.2–1.3 wt.% of Ce_2O_3.

Magnetite has an ulvospinel component that varies widely from 39 to 4% (Appendix 2C). The Mn jacobsite and magnesioferrite components reach 9% and 15% respectively in the carbonatite magnetite. The early crystallization of magnetite in some leucitolites seems to be related to oxidising conditions. It would also be related to the $H_2O/CO_2/F$ ratio in the dissolved fluid phase, but we have no precise information on this ratio and its evolution.

Calcite forms the peperite matrix and is the major mineral of the carbonatite xenolith. Microprobe analysis results (Appendix 2D) show that it is almost pure calcite with very low MgO content even in the carbonatite. However, SrO can reach 2.2 wt.% in the calcite of the carbonatite.

Preliminary geochemical results

Major elements

All the studied felsic rocks belong to strongly silica-undersaturated series, and are foidite-foidolite type rocks (Table 2). Many plutonic xenoliths found in the Eğirdir area have cumulated characters such as the ultramafic pyroxenite with one or two liquidus main phases (clinopyroxene and phlogopite) and the leucitolite xenoliths with two main layered phases (leucite and clinopyroxene). Kamafugite-type xenoliths and feldspath-bearing syenite, exhibiting microgranular or coarse-grained homogeneous textures, are closer to liquid compositions. More appropriate specific classification schemes for ultrapotassic rocks than TAS diagram (Le Maitre 2002) are usually used (Sahama 1974; Foley et al. 1987; Foley 1992b; Woolley et al. 1996).

The microgranular and texturally homogeneous coarse-grained xenoliths (Table 2, Figs. 8, 9) have $MgO \geq 3$ wt.%, $K_2O > 7$ wt.%, and high CaO and are poor in Al_2O_3 and Na_2O (< 1.2 wt.%). They show the lowest value of SiO_2, intermediate values of CaO and K_2O, and are relatively rich in FeOt and TiO_2. They are evolved with a DI (Thornton and Tuttle 1960) > 45 and have no modal olivine like some ultrapotassic plutonic rocks of the Roman Province, Italy (Peccerillo et al. 1984; Peccerillo 1990). They belong to the melilite-, leucite-, and kalsilite-bearing kamafugite group, according to their major element characters (Table 2; Figs. 8, 9). These xenoliths are strongly silica-undersaturated (see CIPW norms, Table 2) with normative leucite, nepheline, and sometimes normative kalsilite. They are very calcic with modal melilite, almost always with normative larnite (sometimes > 10 wt.%) and normative calcite.

The pyroxenite xenoliths are the most enriched in MgO, CaO, and P_2O_5 due to clinopyroxene and apatite (Figs. 8, 9; Table 2). Their variable K_2O is essentially related to the occurrence of phlogopite. They are potentially silica-undersaturated but much less than kamafugite and leucitolite xenoliths (Table 2).

The leucitolite xenoliths plot in the leucitite field (Fig. 9). These rocks are relatively poor in MgO, and extremely rich in K_2O and Al_2O_3, with a very high K_2O/Na_2O ratio (Fig. 9). The opposite variations between K_2O, Al_2O_3, and FeOt, TiO_2, and MgO contents depend on the leucite/mafic phases

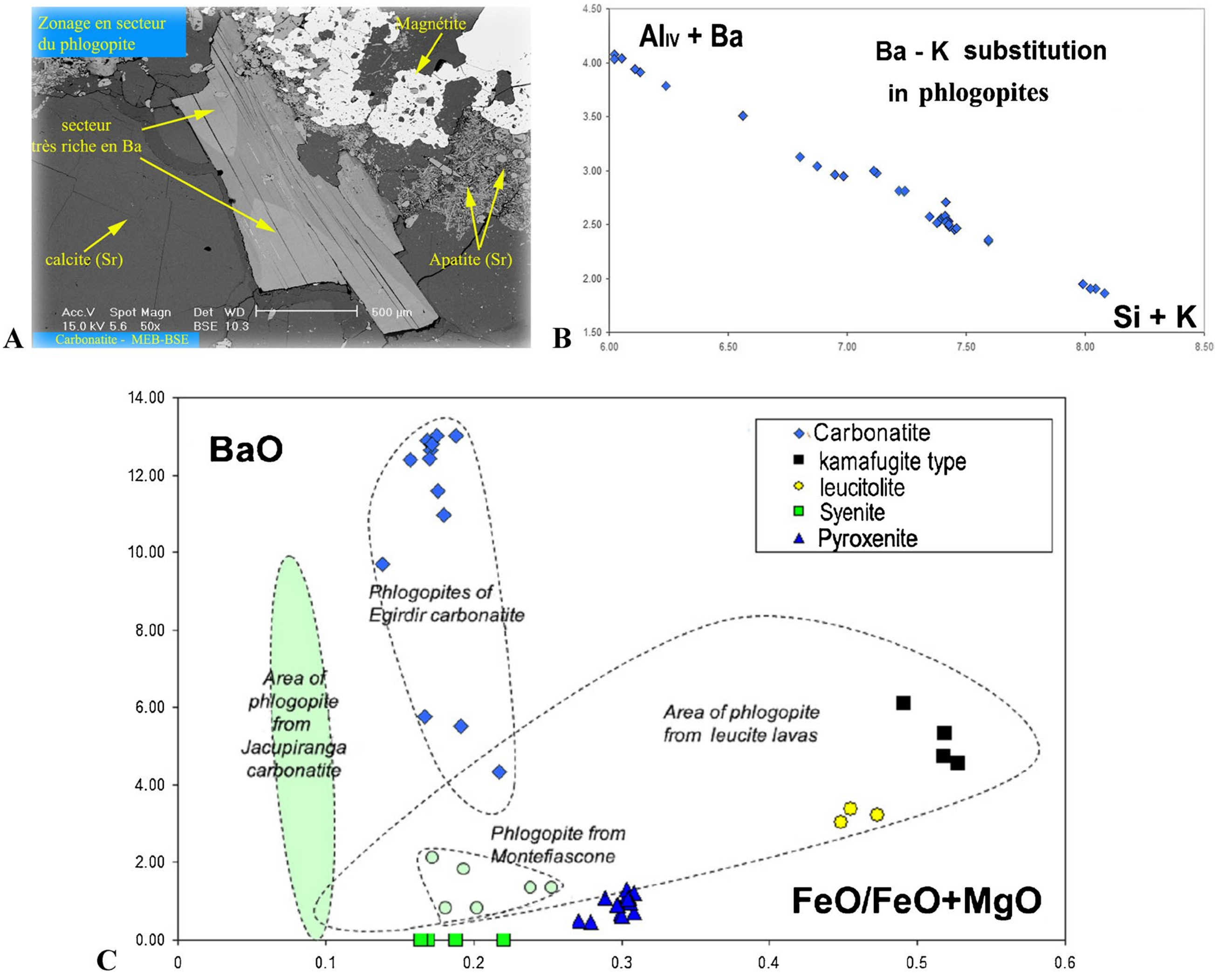

Fig. 7 Composition variations of phlogopite. **A** Sector zoning in phlogopite of the carbonatite xenolith, MEB back-scattered picture. **B** Ba-K substitution in phlogopite from Eğirdir xenoliths. **C** BaO versus FeO/FeO + MgO ratio in phlogopite of carbonatite xenolith and other xenoliths compared to phlogopite of the Jacupiranga carbonatite and phlogopite of leucite lavas (after Gaspar and Wyllie 1982). Green dots, phlogopite of Montefiascone clinopyroxenite, Italy (after Stoppa et al. 2003a, b, c)

(clinopyroxene, garnet, Fe-Ti oxides) ratio in this group, in relation with mineral segregation process. The leucitolite xenoliths (Fig. 9) are always very depleted in Na_2O by comparison to the melilite-bearing leucitites and other previously studied Afyon leucitites (Akal 2003; Prelević et al. 2015).

The observed gaps between the main xenolith groups (Figs. 8, 9) can be related to cumulative processes involving mainly clinopyroxene, apatite, and leucite, as indicated by the textural characteristics of pyroxenites and leucitolites. In almost all Harker diagrams (Fig. 8), the xenoliths from the Alban Hills ejecta, Italy (Peccerillo et al. 1984; Federico et al. 1994) plot in the gap observed between pyroxenite and leucitolite groups. They are P_2O_5-poor compared to the pyroxenite group of Eğirdir. The KLT kalsilitite from Alban Hills ejecta (Figs. 8, 9) plots close to the kamafugite-type xenoliths of Eğirdir. The assumed primary kamafugite "KAM" composition proposed by Prelević et al. (2015) also plots between the pyroxenite and leucitolite groups (Fig. 9).

The hyalophane-bearing syenite and Eğirdir leucitite compositions are close to the leucitolite group, but with lower K_2O and TiO_2 + FeOt values.

The carbonatite xenolith is very poor in Na_2O and MgO (Table 2) and belongs to the calcio-carbonatite type. The P_2O_5 is very high (2.58 wt.%) due to the presence of apatite clusters, which must be considered for the interpretation of REE and other trace elements in the rock.

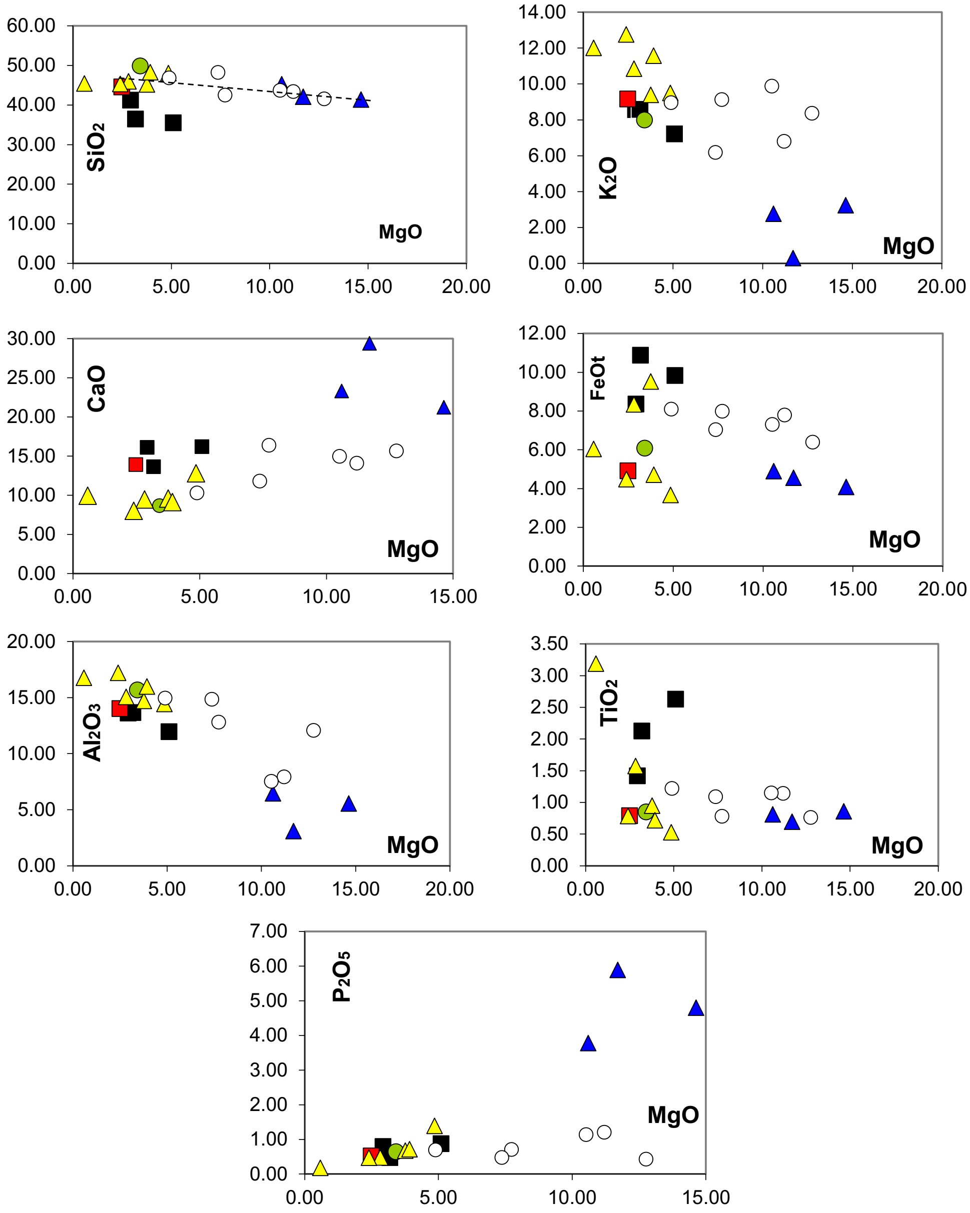

Fig. 8 Major elements versus MgO. Blue triangle, pyroxenite. Yellow triangle, leucitolite. Black square, kamafugite type. Red square, hyalophane-bearing syenite. Green dot, Egirdir leucitite. Open dot, plutonic xenoliths from the Alban Hills Ejecta, Italy

Trace elements

The spidergrams normalized to the primitive mantle (Fig. 10A) for trace elements (Table 2) are used for the feldspar-bearing syenite, leucitites, and kamafugite-type xenoliths that are close to liquid compositions. The syenite and leucitite patterns are very similar, and show a relatively high LILE to HFSE ratio. The negative Ta, Nb, and Ti anomalies are present but are moderate (weak in the case of Hf), while Zr displays a weak positive anomaly. The kamafugite-types display the same negative anomalies. They are globally enriched in REE relative to the syenite and leucitite. The negative Sr anomaly is particularly pronounced for two kamafugite-type xenoliths, probably related to early apatite fractionation. All the rocks have a prominent Pb positive peak. All these geochemical features have been also noted for ultrapotassic magmatism of the Roman Province, Italy (Conticelli et al. 2013, 2015). They are related to an orogenic or post-orogenic signature with a crustal material assimilation into the upper mantle during a previous subduction process. However, there are some discrepancies: Ba is not very depleted and there is no clear positive Th and Cs peaks. The same geochemical characters have been observed in the Ultrapotassic-Potassic Afyon volcanic Province (Prelević et al. 2015). The trace element patterns of the studied xenoliths are very different from those of intraplate ultrapotassic rocks, similar to the Roman Province (Conticelli et al. 2015). Looking at the REE patterns (Fig. 11), kamafugite-type

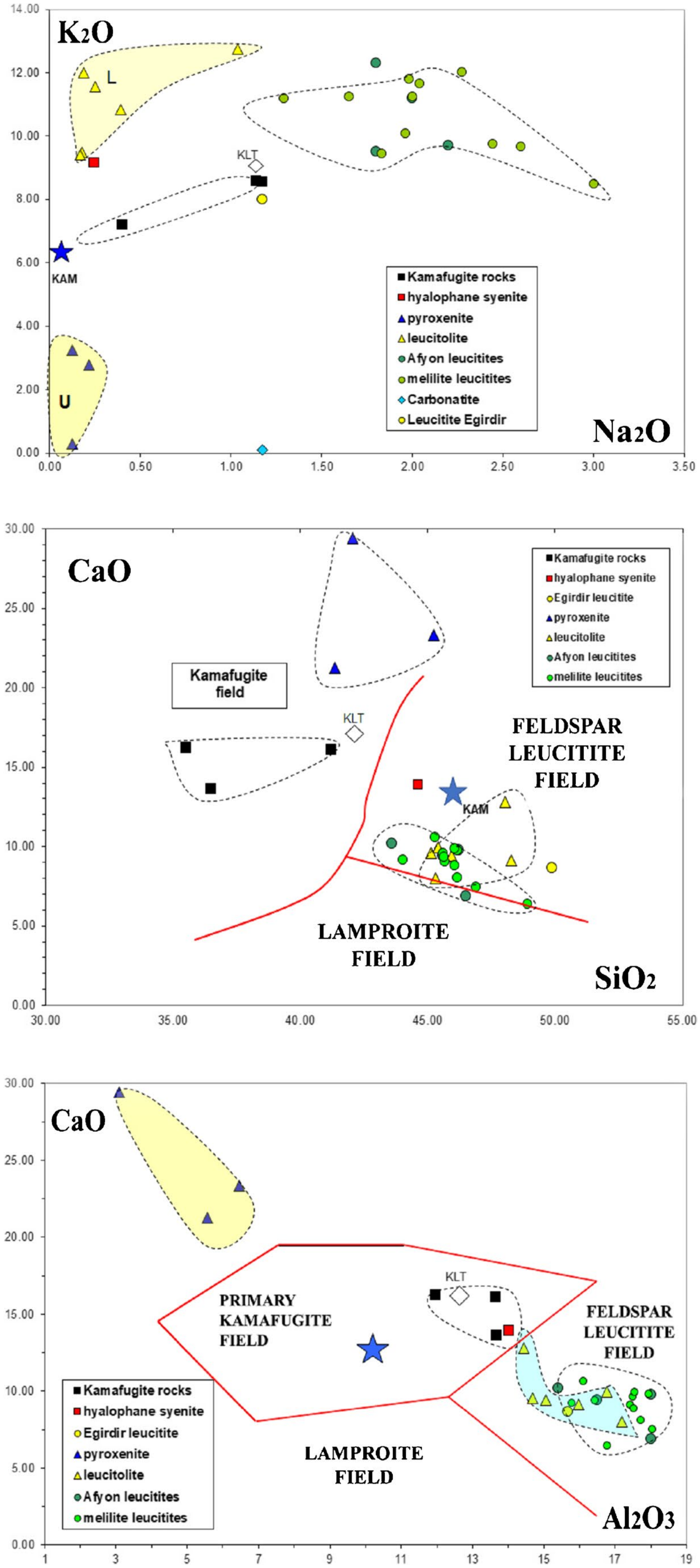

Fig. 9 Major element diagram with kamafugite, leucitite and lamproite fields after Foley (1987). Blue star, assumed primary kamafugite magma after Prelević et al. (2015). Open diamond, KLT kalsilitolite xenolith from Alban Hills ejecta (Federico et al. 1994). Afyon leucitites are from Prelević et al. (2015). Melilite leucitite are from Akal (2003), Akal et al. (2013)

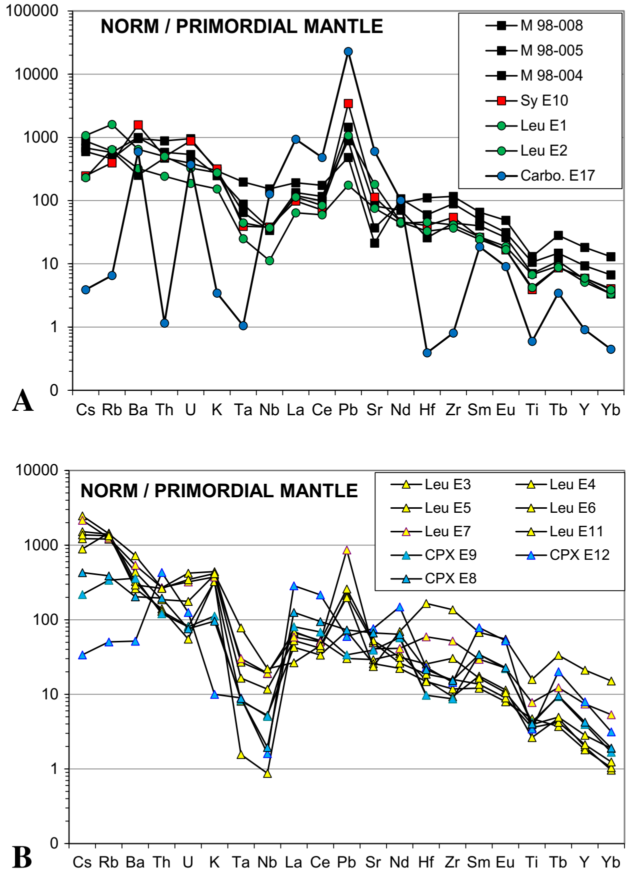

Fig. 10 Trace elements normalized to primordial mantle. **A** Patterns of kamafugite-type (M, black squares), syenite (Sy), leucitite (Leu), and carbonatite (Carbo) xenoliths. **B** Patterns of leucitolite (Leu) and clinopyroxenite (CPX) xenoliths. Normalizing values from Sun and McDonough (1989)

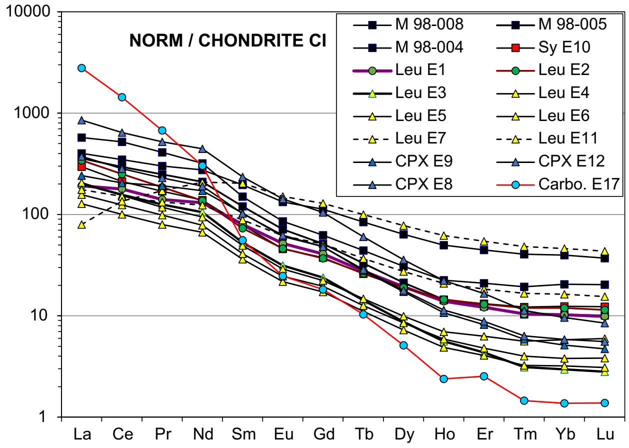

Fig. 11 REE/chondrite CI normalized patterns. Same rock references as Fig. 10

xenoliths are enriched in REE, especially HREE, compared to leucitite and syenite (Figs. 10, 11). All the trends show no positive or negative Eu anomaly.

Spidergrams are less suited to xenoliths involving cumulative processes (pyroxenite and leucitolite xenoliths), but the patterns provide a simple overall view of the main trace elements and can show the possible effects of mineral fractionation on the parent liquids. The pyroxenite xenoliths are depleted in HFSE, Pb, and LILE (including Pb) relative to REE and have enriched HREE relative to LREE, due to their high but variable modal apatite and pyroxene fractions (Figs. 10B, 11). They are Th-enriched. Rb and Ba are variable and enriched together with K in two pyroxenites, due to the third mineral to crystallize which is phlogopite.

The trace element patterns of the leucitolite xenoliths are globally similar (Figs. 10B, 11) and characterized by a global depletion in REE, Ta, Nb, and Ti when compared to the patterns of leucitite and kamafugite type. The leucitolites are globally enriched in LILE relative to pyroxenites, and K. However, notable variations of HFSE troughs and HREE/LREE ratio in this leucitolite group seem to be very dependent upon the leucite/clinopyroxene ratio and garnet content. Two garnet-rich leucitolites (Fig. 11) are strongly enriched in HREE, Zr, and Hf relatively to LREE. The role of garnet is probably crucial for these samples, and is consistent with the trace element patterns of garnet published by Prelević et al. (2015). A prominent peak of Pb is always seen for the most leucite- and garnet-enriched leucitolites, which is a difference with the pyroxenite group.

The trace element pattern of the carbonatite (Figs. 10A, 11) shows a strong LREE/HREE fractionation pattern and is very depleted in HFSE, except for Nb, and is also depleted in K, Rb, and Th relative to U and Ba. It has the most prominent Pb peak. This pattern has nothing to do with that of intraplate carbonatites, but shows similarities with those of sandstones, pelites, and especially limestones of the past and present Mediterranean alpine area (see the trends published by Conticelli et al. (2015 and ref. wherein)), with very high peaks for U, Pb, and Sr and deep troughs for K, Ta, Hf, Zr, and Ti. However, apatite, which forms clusters in the carbonatite xenolith, is the first mineral that can explain the LREE/HREE enrichment of the carbonatite. Moreover, the spidergrams of apatite from the Potassic Ultrapotassic Afyon volcanic Province (Prelević et al. 2015) show the same LREE/HREE enrichment and deep troughs for Ti, Zr, Ta, and Rb. The only discrepancy concerns Th, which is very low in this carbonatite xenolith. This depletion eventually may be linked to pneumatolytic reworking and escape of Th during the phreatomagmatic event, a process that could be considered as viable for a 10-cm-sized xenolith.

Stable isotope data on calcite

^{18}O and ^{13}C stable isotope analyses have been carried out on calcite extracted from the carbonatite xenolith, the peperite matrix, the hyalophane-bearing syenite, and two limestones from the surrounding basement that has been cut and covered by the volcanoclastic deposit (Table 3, Fig. 12). Analyses are reported on the **δ**^{18}O versus **δ**^{13}C diagram (after Bell 2005; Doroshkevich et al. 2010). The **δ**^{13}C isotopic signatures of calcite from the carbonatite xenolith, the peperite matrix, and the hyalophane-bearing syenite are negative and are distinct from the **δ**^{13}C measured on the limestones from the basement. The **δ**^{13}C and **δ**^{18}O values of the carbonatite are close to the limit values for the primary carbonatite field (PCF, Fig. 12). This means that a mantle signature, with slight modification by fractionation or contamination, can be considered for the carbonatite xenolith. Similarly, the **δ** ^{13}C of the calcite found in the syenite is also compatible with a primary origin of the CO_2-rich fluid component dissolved in the magma parent and plots within the so-called European carbonatite field. However, the **δ**^{18}O is significantly higher, which can be ascribed to a contamination during a low-temperature alteration process. The **δ**^{18}O of the peperite matrix is much higher and disconnected from its **δ**^{13}C that remains low, which can be ascribed to a main contamination process at a low temperature involving meteoritic H_2O during the volcanic event. A carbonatitic fluid interaction has been proposed in some peperite belonging to the Cenozoic French Limagne phreatomagmatism (Bailey et al. 2006; Chazot and Mergoil-Daniel 2012), which is an alternative

Table 3 **δ**1^{3}C and **δ**^{18}O stable isotope measures on carbonates

Rock sample	Processing	d13C/PDB	d18O/PBD	d18O/SMOW*	Mineral specificity
E17 carbonatite	H3PO4 24 h à 25 °C	-4.60	-17.76	12.60	calcite
E17 carbonatite	H3PO4 15 Days at T = 25 °C	-4.60	-17.82	12.54	calcite + Mg-carbonate
E10 syenite	H3PO4 15 Days at T = 25 °C	-5.30	-13.81	16.67	calcite + Mg-carbonate
E10 syenite	H3PO4 24 h at T = 100 °C	-5.55	-14.94	15.51	all carbonates
SE17 limestone	H3PO4 15 Days at T = 25 °C	1.94	-2.34	28.50	calcite + Mg-carbonate
SE08 limestone	H3PO4 15 Days at T = 25 °C	-0.83	-6.41	24.30	calcite + Mg-carbonate
PEP peperite matrix	H3PO4 15 Days at T = 25 °C	-6.8	-9.65	20.96	calcite + Mg-carbonate

δ^{18}O SMOW calculated after Coplen et al., 1983. Measure precisions: **δ**^{13}C/PDB ± 0.1; **δ**^{18}O/PBD ± 0.2

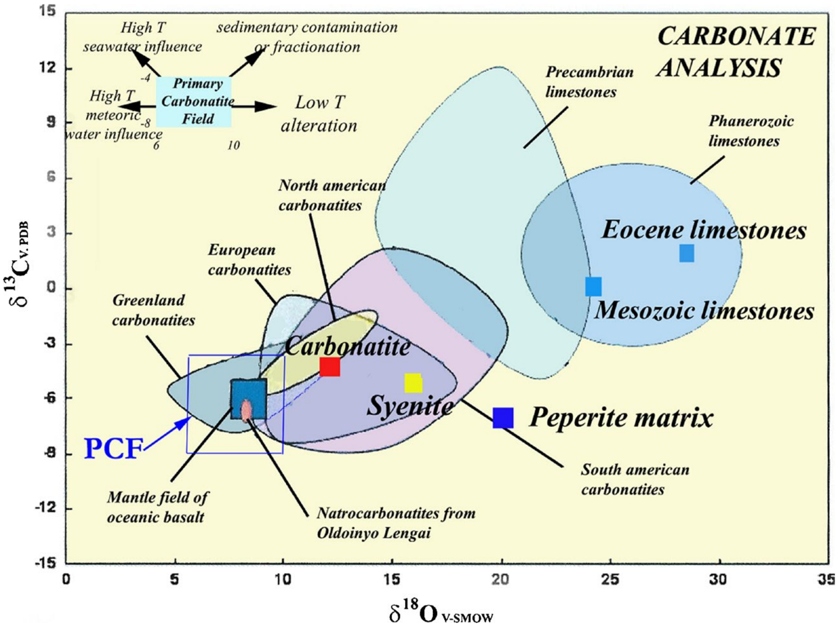

Fig. 12 **δ**^{13}C versus **δ**^{18}O stable isotope composition of calcite from xenoliths and limestones. Calcite has been extracted from two plutonic xenoliths (carbonatite and syenite), the peperite matrix at the bottom of the volcano-clastic deposit, and two limestones (Mesozoic limestone and Eocene lacustrine) of the surrounding basement. PCF, primordial carbonatite field

from the classical origin of peperite. It is difficult to rule out the prevalent low-T interaction process between the leucitite magma, meteoritic water, and limestones or lacustrine that raises the δ^{18}O but not the δ^{13}C for the calcitic matrix of the peperite. In the other hand, the low δ^{13}C can also be explained by the presence of a juvenile CO_2-rich fluid in relation with the leucitite lava or/and a separate carbonatitic magma.

Discussion

Xenolith mineral parageneses and their origin

Textures and restricted mineral paragenesis of pyroxenites and leucitolites (one to three euhedral major phases), and geochemical gaps existing between pyroxenites and leucitolites on the one hand, and syenite, kamafugites, and leucitites on the other hand, suggest that pyroxenites and leucitolites are assumed to be cumulates derived from underlying magma intrusions. The term of autolith would be better than xenolith for these two groups of rocks as it has been used for the autoliths from the Kilombe volcano, Kenya Rift, and the Ilimaussaq autoliths, Greenland (Ridolfi et al. 2006; Schönenberger et al. 2006). Cumulate-type rocks are known in ultrapotassic provinces, such as the Malawi ring complexes, in particular the ultrapotassic Mlindi ring complex (Laval and Hottin 1992). Trace element patterns of pyroxenite and leucitolite also show that their bulk compositions are a direct expression of the ratio of mafic and felsic mineral. Apatite, clinopyroxene, phlogopite, and leucite are the major mineral phases that crystallized in the magma at depth, in good agreement with the differentiation process suggested by Prelević et al. (2015).

Small xenoliths of kamafugite affinity are very enriched in early melilite crystals and some leucitolite cumulates are very garnet-enriched, which suggests that some garnet- or melilite-enriched segregations or layers formed during their crystallization.

Kamafugite-type and syenite xenoliths show homogeneous fine-grained porphyritic textures, a common feature observed not only in small dykes, but also on the chilled margins of intrusions. Coarse-grained kamafugite-type xenoliths never show layering features or crystal segregation, indicating that they probably represent evolved liquids injected and crystallized at depth in the crust.

Implications of experimental studies

The variable mineral paragenesis of the studied xenoliths is relevant to the complex system kalsilite-forsterite-larnite-quartz tetrahedron and related subtetrahedra (Yoder 1986; Gupta 2015) and has been experimentally investigated for a long time (Gupta et al. 2006; Edgar et al. 1976; Gupta and Yagi 1980; Veksler et al. 1998; Gupta 2015 and ref. wherein). In the Eğirdir xenoliths, the presence of phlogopite and lack of olivine fit well in the phlogopite-kalsilite-clinopyroxene-leucite-melilite-feldspar sub-tetrahedra, with mutual exclusion between melilite and feldspar, as it is observed in melilite-bearing kamafugite-type and feldspar-bearing syenite xenoliths. However, the natural paragenesis system is more complicated than the experimental system because Fe and Ti were not considered. The later elements probably complicated the paragenesis with crystallization of FeTi-oxides and garnet. Heteromorphic relations with incomplete reactions (Yoder 1986) in kamafugite magmas can also complicate the paragenesis of the rocks during crystallization.

Conditions of crystallization and fractionation processes

The modal variations depicted in the xenoliths show that the early crystallizations of melilite, clinopyroxene, apatite, and phlogopite, followed by leucite, play the major role in the differentiation process, in good agreement with experimental studies.

Early crystallization of phlogopite rather than olivine in phlogopite-bearing pyroxenite cumulates, and early Ti-Fe oxides associated with clinopyroxene phenocrysts in subvolcanic kamafugite-type are symptomatic of relatively elevated partial P_{H2O} and oxidizing conditions during crystallization.

It is difficult to specify from which magmatic bodies (depth and size) the rock samples have been extracted, when they only consist of a set of xenoliths. The leucitite lava was responsible for their extraction and we consider that leucitite represents the last magma passing through the previous crystallized intrusions and dykes, being the residual magma coming from the crystallizing intrusions and lately injected towards the surface. The stability field of leucite in the presence of dissolved water is restricted when the pressure increases, leucite being finally removed beyond 0.8 GPa (Fudali 1963; Gittins et al. 1980 and references therein). The systematic occurrence of leucite in the xenoliths, even in pyroxenite, indicates that the xenoliths have crystallized under relatively low P_{H2O}, not above the 0.3–0.8 GPa range, i.e., at a maximum depth of 25 km. This maximum depth corresponds to the xenoliths showing frequent and early crystallization of phlogopite (Prelević et al. 2015).

Calcite crystallization depends not only on the composition and evolution of the dissolved fluid phase in magma, but also on the low-temperature alteration processes. This is true for the calcite-bearing syenite xenoliths and for the kamafugite-type xenoliths. In the CO_2 vs CaO diagram (Appendix 3), CO_2 is higher in the kamafugite and syenite xenoliths than in the pyroxenite and leucitolite cumulates (see Table 2). The kamafugite and syenite evolved liquids appear to be enriched in CO_2 relative to H_2O. Early phlogopite fractionation may have increased the CO_2/H_2O ratio in the dissolved fluid phase.

As explained by Yoder (1986) and McBirney (1984) for the Ultrapotassic Shonkin sag laccolith (Montana), it is difficult to explain the relationships between all types of rocks by a single fractional crystallization process from a single primary magma; in addition, Eğirdir xenoliths are not demonstrated to be all cogenetic. Other processes could also operate during the crystallization of intrusions: (i) percolation-reaction of the residual melt through the cumulates by infiltration metasomatism, as it is assumed in the mafic–ultramafic cumulates of layered intrusions near the solidus (Irvine 1980; Tait et al. 1984; Sparks et al. 1985; Brandeis and Jaupart 1986; Boudreau 1995); (ii) volatile transfer of Na relative to K explaining why the leucitolite cumulates are very depleted in Na_2O (McBirney 1984; Peccerillo 1994); (iii) mobile pneumatophile elements such as Th, during the hydrothermal activity at low pressure, and percolation of a CO_2-rich fluid phase exsolved from the residual magma.

The evolution trends may be illustrated in the $CaO/K_2O/Fe_2O_3$ ternary diagram (Fig. 13). The primary melts are unknown. The less evolved KAM mafic magma assumed by Prelević et al. (2015) is close to the intermediate and salic ejecta found in the Alban Hill, Italy, especially the KLT kalsilitite xenolith (Lacroix 1893, 1917; Conticelli and Peccerillo 1992; Federico et al. 1994). The Eğirdir kamafugite seems to be more evolved and may be the result of efficient clinopyroxene and leucite fractionation, leading to iron enrichment relative to CaO and K_2O, being thus related to the two main groups of Eğirdir cumulates (pyroxenite and leucitolite). The evolution represented by the leucitite lava is mainly controlled by leucite fractionation, with iron content remaining globally constant, and is related to the crystallization of garnet and Fe-Ti oxides. The resulting liquid line of descent is questionable as not all xenoliths are cogenetic, especially the kamafugite-type and syenite xenoliths, which are most likely related to two different magmas. If a reasonable liquid line of descent exists, it should be restricted from kamafugite to leucitite magmas in relation to the trend of assumed cumulates shown in this ternary diagram.

Carbonatite xenolith significance and hypothetic origin

The association of carbonatite and kamafugite magmas is known elsewhere in ultrapotassic magmatism, where blobs of calcio-carbonatite and kamafugite can be intimately associated. This relationships between two contrasted carbonate–silicate conjugates have been described for example in magmatic rocks of the Mahlber complex, Germany (Solovova et al. 2003), in the West Qinling Province, China (Yu et al. 2003; Guo et al. 2014), in the Ruri Volcano, Kenya (Stoppa et al. 2003b), and in the Roman Province and Intra-mountain Ultra-alkaline Province, Italy (Stoppa et al. 2003a). In the Potassic Ultrapotassic Afyon volcanic Province, this intimate association has been observed in leucite-bearing phonolites (Elitok 2019). This close association between carbonatite and

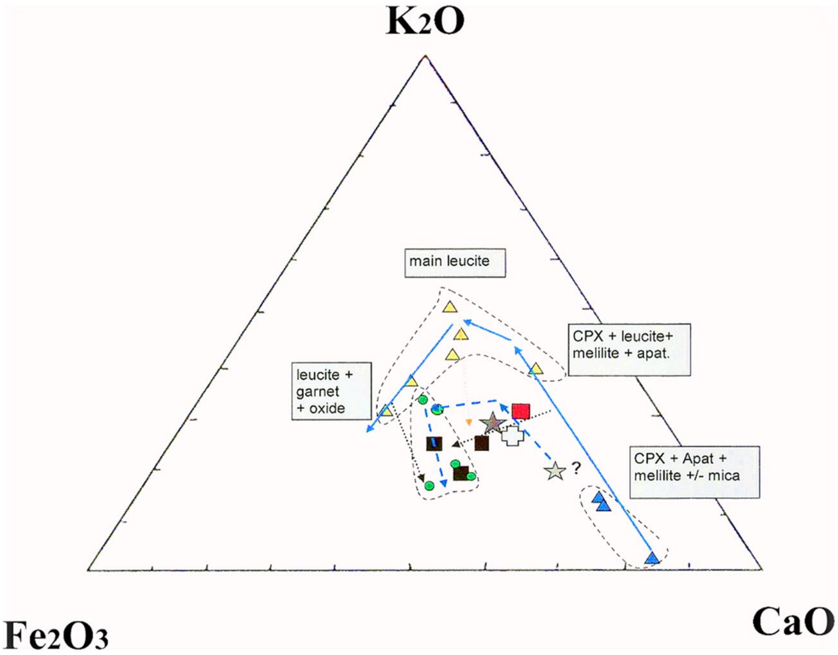

Fig. 13 K_2O-Fe_2O_3-CaO ternary diagram. Blue triangle, pyroxenites; yellow triangle, leucitolites; black square, kamafugite type; red square, hyalophane-bearing syenite; small green dots, leucitites of Afyon ultrapotassic series (after Prelević et al. 2015); large green dot, leucitite of Egirdir. Green star, KAM assumed primary kamafugite magma (Prelević et al. 2015); white cross, KLT kalsilitolite xenolith from Alban Hills ejecta (Federico et al. 1994); gray star, hypothetic primary mafic magma. Blue arrows trend of successive cumulates; blue broken arrows, hypothetic magma evolution trend. The fractionation process would be governed by the mineral phases in the successive boxes

very silica-undersaturated rocks has been attributed to an immiscibility process between carbonatite and silicate liquids. This immiscibility model between two silicate-carbonate conjugates has been experimentally tested at a relatively low pressure from < 0.1 to 0.5 GPa (Koster van Groos and Wyllie 1966; Wyllie 1987; Kjarsgaard and Hamilton 1988; Lee and Wyllie 1998). Eğirdir xenoliths and their set of rock-forming minerals are plotted in the silica-alkali-carbonate diagram where the immiscibility fields are reported (Fig. 14) after Kjarsgaard and Hamilton (1988). The two arrows drawn from leucitolites and pyroxenites show that these cumulates can lead to the Eğirdir kamafugite through immiscibility in the 0.1–0.5-GPa pressure range. However, the theoretical conjugate carbonatitic liquid does not fit with the calcio-carbonatite xenolith found at Eğirdir: in this model, the composition of the Eğirdir carbonatite would require an additional process of accumulation of calcite and apatite crystals.

Another model for the genesis of the Eğirdir calcio-carbonatite would be to consider a direct interaction of the leucitic magma with the limestone basement (Elitok 2019).

Phreatomagmatic interaction with limestone basement or lacustrine carbonate during the explosive eruption could explain the calcitic matrix of the breccia occurring within the pipe and the peperite from the bottom of the Eğirdir phreatomagmatic deposit. However, stable isotope compositions of calcite from the Eğirdir carbonatite indicate low crustal contamination. It seems that the origin of the Eğirdir carbonatite differs from the result of interaction between the leucitic magma with the limestone basement.

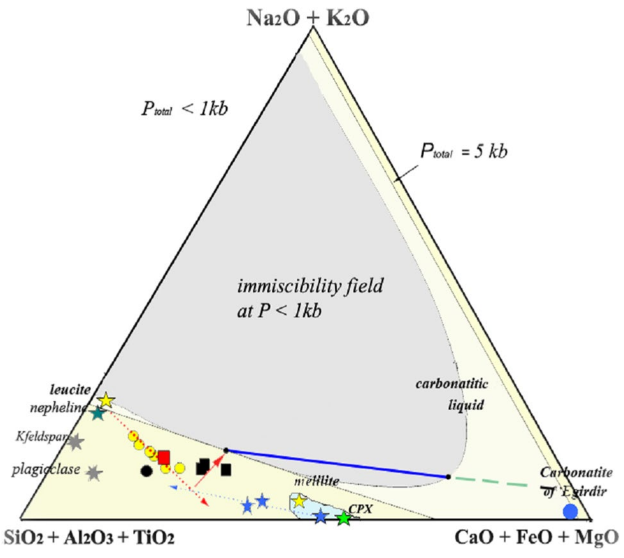

Fig. 14 Liquid immiscibility fields for Pt < 0.1 GPa and Pt = 0.5 GPa, in the $SiO_2 + Al_2O_3 + TiO_2$ – $Na_2O + K_2O$ – $CaO + FeO + MgO$ ternary diagram. Blue stars, pyroxenite xenoliths; other stars, mineral phases. Black squares, kamafugite-type xenoliths; red square, hyalophane-bearing syenite; black dot, Egirdir leucitite; yellow dot, leucitolite xenoliths. Blue straight line, conjugate silicate-carbonate liquids at $P < 0.1$ GPa. Green dashed line, conjugate liquids at 0.5 GPa (after Kjarsgaard and Hamilton 1988). Blue and red dotted lines with arrows, effect of leucite and clinopyroxene during fractional crystallization; the two trends cross at the average cumulate

Globally, the composition of the Eğirdir calcio-carbonatite does not correspond to the intraplate carbonatite compositions related to HIMU and EM1 mantle components (Simonetti and Bell 1994; Woolley 2003; Tappe et al. 2003; Bell and Simonetti 2009) or to a direct CO_2-enriched fluid produced during the asthenosphere upwelling after the breakoff of the slab.

The composition of the Eğirdir carbonatite xenolith is more consistent with carbonatites found in an orogenic or post-orogenic geodynamical setting. The coexistence of ultrapotassic rocks and carbonatite has been a subject of debate for a long time (Foley 1992a, 1992b; Peccerillo 1984, 1998; Vollmer 1989; Peccerillo and Foley 1992; Ersoy et al. 2010; Prelević et al. 2008, 2010a, 2010b, 2012, 2015; Conticelli 1998; Conticelli et al. 2007, 2013, 2015). In a post-collisional geodynamical situation, the carbonatite mantle source would be phlogopite-bearing pyroxenite veins formed in a moderately depleted lithospheric mantle metasomatized by the fluid released by the sediments of the subducted slab. There is also a possibility to produce a carbonatitic melt by a fractionation-melting process of the metasomatized mantle source: this origin for carbonatite was proposed by Mitchell (2005). More extensive partial melting of the same source may product primary lamproite or kamafugite magmas, with high K/Na ratio, and high Ca, Mg, and CO_2 contents related to the metasomatized source. The differentiation process can also be at the origin of carbonatite: indeed, after extensive differentiation of melilitite and nephelinite magmas, a carbonatite residue may be produced (Mitchell 2005).

The mantle source of the UKAP magmatism and its complex metasomatization have been debated in the successive papers of Prelević et al. (2008, 2010a, b, 2012, 2015). Future isotopic studies of the Eğirdir xenoliths will be of great help to better understand the origin and relationships of these plutonic xenoliths with the Potassic Ultrapotassic Afyon volcanic Province, and to clarify whether they have fully or partially preserved their complex mantle geochemical signature, despite contamination processes during crustal magma injection and differentiation.

Concluding remarks

The plutonic xenoliths found in the Eğirdir phreatomagmatic deposits have been extracted from dykes or/and plutonic intrusions related to batches of magma injected at crustal level.

Pyroxenite or leucitolite cumulates were formed during the differentiation of these crustal intrusions under a maximum P_{total} of 0.8 GPa corresponding to a maximum depth of 25 km. These rocks are assumed to be autoliths.

Eğirdir xenoliths are related to the strongly silica-depleted ultrapotassic series of West Anatolia. Some of them have kamafugite affinities and display the first occurrence of kalsilite in this ultrapotassic series. Two forms of kalsilite have been observed: a high-T hypersolvus homogeneous form symptomatic of rapid cooling, and a subsolvus low-T exsolved form associated with separate nepheline crystals in slow-cooling intrusions. In syenite, feldspar crystallized first as hyalophane, which played the same role of nepheline during the leucite destabilization in K- and Ba-rich, and Na-poor magmas.

The mineral paragenesis that controlled the fractional crystallization process was mainly composed of clinopyroxene apatite, melilite, phlogopite, and leucite, with additional garnet and Fe-Ti oxides during the near-solidus evolution of leucitolite cumulates. Phlogopite crystallization in some pyroxenite indicates that partial P_{H2O} was high during their crystallization, leading to an increase of the CO_2/H_2O ratio in the dissolved fluid phase.

The trace elements of the investigated xenoliths corresponding to liquid compositions (kamafugite and syenite types) indicate an orogenic/post-orogenic geodynamical setting as assumed for the Potassic Ultrapotassic Afyon volcanic Province (Prelević et al. 2008, 2015) and the Roman Province, Italy (Peccerillo 1990; Conticelli et al. 2013).

A carbonatite xenolith has been found for the first time in this area. There are no convincing petrographic arguments to support an immiscibility process between two silicate-carbonate conjugates. C and O stable isotopic compositions on calcite indicate that the carbonatite has a mantle origin with relatively limited crustal contamination. The origin of the carbonatite by differentiation from a primitive kamafugite-type magma, or by a fractionation-melting process of a metasomatized mantle source remains to be tested in the future.

New isotopic data on Eğirdir xenoliths, especially on carbonatite- and kamafugite-type xenoliths, are needed to better understand their origin, their possible cogenesis, and mantle sources.

Supplementary Information The online version contains supplementary material available at https://doi.org/10.1007/s12517-023-11766-7.

Acknowledgements Special thanks to E. Chassefière, past head of the GEOPS research team, N. Özgur, and F. Yağmurlu past dean of the Sûleyman Demirel University. M. Fialin and N. Rividi are thanked for microprobe analysis assistance at Camparis Lab., Université Paris-Sorbonne, also V. Godard for the excellent polish fine sections. L. Weinberg is thanked to improve the English language. An anonymous reviewer is thanked for his comments on an earlier version of the manuscript. J.P. Liégeois is warmly thanked for careful review of the manuscript.

Funding This work was financially supported by the UMR CNRS 8148 GEOPS, Dpt. Sciences de la Terre, Université Paris-Saclay, and the Sûleyman Demirel University, Isparta, Turkey for field work support and accommodations.

Declarations

Conflict of interest The author(s) declare that they have no competing interests.

References

Akal C (2003) Mineralogy and geochemistry of melilite leucitites, Balçıkhisar, Afyon (Turkey). Turk J of Earth Sci 12:215–239

Akal C, Helvaci C, Prelević D, van den Bogaard P (2013) High-K volcanism in the Afyon region, western Turkey: from Si-oversaturated to Si-undersaturated volcanism. Int J Earth Sci 102:435–453

Alici P, Temel A, Gourgaud A, Kieffer G, Gündoğdu MN (1998) Petrology and geochemistry of potassic rocks in the Gölcük area (Isparta, SW Turkey): genesis of enriched alkaline magmas. J Volc Geoth Res 85(1–4):423–446

Aurisicchio C, Federico M (1985) Nepheline - kalsilite microperthites in ejecta from the Alban Hills (Italy). Bull Geol Soc Finl 57(1–2):129–137

Bailey K, Kearns S, Mergoil J, Mergoil-Daniel J, Paterson B (2006) Extensive dolomitic volcanism through the Limagne Basin, central France: a new form of a carbonatitic activity. Mineral Mag 70:1–6

Beccaluva L, Di Girolamo P, Serri G (1991) Petrogenesis and tectonic setting of the Roman volcanic province. Italy Lithos 26(3–4):191–221

Beccaluva L, Bianchini G, Wilson M (eds) (2012). Cenozoic volcanism in the Mediterranean Area. Geol. Soc. Am. Spec. Paper 418, 171-202.

Bell K (2005) Carbonatites. In: Selley RC, Cocks LRM, Plimer IR (eds) Encyclopedia of Geology. Elsevier, Amsterdam, pp 217–233

Bell K, Powell JL (1969) Strontium isotopic studies of alkalic rocks: the potassium-rich lavas of the birunga and Toro—Ankole Regions, East and Central Equatorial Africa. J Petrol 10:536–572

Bell K, Simonetti A (2009) Source of parental melts to carbonatites-critical isotopic constraints. Mineral Petrol 98(1):77–89

Bell K, Tilton GR (2001) Nd, Pb and Sr isotopic compositions of East African carbonatites: evidence for mantle mixing and plume inhomogeneity. J Petrol 42:1927–1945

Bergman SC (1987). Lamproites and other potassium-rich igneous rocks : a review of their occurrence, mineralogy and geochemistry. In Fitton JG., Upton BG (eds). Alkaline igneous rocks, Geol. Sci. Special Pub., 30, 103–190.

Boudreau AE (1995) Crystal aging and the formation of fine-scale layering. Mineral Petrol 1995(54):55–69

Brandeis G, Jaupart C (1986) On the interaction between convection and crystallization in cooling magma chambers. Earth Planet Sci Lett 77:345–361

Caran S (2016) Mineralogy and petrology of leucite ankaratrites with affinities to kamafugites and carbonatites from the Kayıköy area, Isparta, SW Anatolia, Turkey: implications for the influences of carbonatite metasomatism into the parental mantle sources of silica- undersaturated potassic magmas. Lithos 256–257:13–25

Carmichael IS, Turner J, Verhoogen J (1974). Igneous petrology. McGraw-Hill, 739.

Çoban H, Topuz G, Roden MF, Hoang N, Schwarz WH (2019) ^{40}Ar-^{39}Ar dating and petrology of monzonite ejecta in tephra from Quaternary Gölcük volcano (Isparta, SW Turkey): tear-related contrasting metasomatic symptoms in extensional mantle-derived magmas. Lithos 330–331:160–176

Chazot G, Mergoil-Daniel J (2012) Co-eruption of carbonate and silicate magmas during volcanism in the Limagne graben, French Massif Central. Lithos 154:130–146

Conticelli S, Peccerillo A (1992) Petrology and geochemistry of potassic and ultrapotassic volcanism in Central Italy: petrogenesis and inferences on the evolution of the mantle sources. In: Peccerillo A, Foley S (eds) Potassic and ultrapotassic magmas and their origin. Lithos 28:221–240

Conticelli S (1998) The effect of crustal contamination on ultrapotassic magmas with lamproitic affinity: Mineralogical, geochemical and isotope data from the Torre Alfina lavas and xenoliths, Central Italy. Chem Geol 149:51–81

Conticelli S, Carlson RW, Widom E, Serri G (2007) Chemical and isotopic composition (Os, Pb, Nd, and Sr) of Neogene to Quaternary calc-alkalic, shoshonitic and ultrapotassic mafic rocks from the Italian Peninsula: inferences on the nature of their mantle sources. Spec Paper Geol Soc Am 418:171–202

Conticelli S, Avanzinelli R, Poli G, Braschi E, Giordano G (2013) Shift from lamproite-like to leucititic rocks: Sr-Nd-Pb isotope data from the Monte Cimino volcanic complex vs. the Vico stratovolcano. Central Italy Chem Geol 353:246–266

Conticelli S, Avanzinelli R, Ammannati E, Casalini M (2015) The role of carbon from recycled sediments in the shift from lamproite to leucitite in the Central Mediterranean region. Lithos 232:174–196

Cundari A (1979) Petrogenesis of leucite-bearing lavas in the Roman volcanic region, Italy. Sabatini Lavas Contrib Mineral Petrol 70:9–21

Di Battistini G, Montanini A, Vernia L, Venturelli G, Tonarini S (2001) Petrology of melilite-bearing rocks from the Montefiascone volcanic complex (Roman Magmatic Province): new insights into the ultrapotassic volcanism of Central Italy. Lithos 59(1–2):1–24

Doroshkevich AG, Ripp GS, Moore KR (2010) Genesis of the Khaluta alkaline-basic Ba-Sr carbonatite complex (West Transbaikala, Russia). Miner Petrol 98:245–268

Edgar AD (1992) Barium-rich phlogopite and biotite from some Quaternary alkali mafic lavas, West Eifel. Germany Eur J Mineral 4:321–330

Edgar AD, Arima M (1981) Geochemistry of three potassium-rich ultrabasic lavas from the west branch of the African rift: inferences on their genesis. Neues Jb Mineral Monatsh 12:539–552

Elitok Ö (2019) Geology and petrology of the potassic and ultrapotassic rocks from the northern part of Senirkent (Isparta-SW Turkey): evidence of magma–carbonate wall-rock interactions. Arab J Geosci 12:1–23

Ersoy EY, Helvaci C, Palmer MR (2010) Mantle source characteristics and melting models for the early-middle Miocene mafic volcanism in Western Anatolia: implications for enrichment processes of mantle lithosphere and origin of K-rich volcanism in post-collisional settings. J Volc Geotherm Res 198:112–128

Essene EJ, Clafin CL, Giorgetti G, Mata PM, Peacor DR, Arkai P, Rathmell MA (2005) Two-, three- and four-feldspar assemblages with hyalophane and celsian: implications for phase equilibria in $BaAl_2Si_2O_8$-$CaAl_2Si_2O_8$-$NaAlSi_3O_8$-$KAlSi_3O_8$. Eur J Mineral 17:515–535

Federico M, Peccerillo A, Barbieri M, Wu TW (1994) Mineralogical and geochemical study of granular xenoliths from the Alban Hills volcano, Central Italy: bearing on the evolutionary processes in potassic magma chambers. Contrib Mineral Petrol 115:384–401

Ferguson AK, Cundari A (1982) Feldspar crystallization trends in leucite-bearing and related assemblages. Contrib Mineral Petrol 81:212–218

Foley SF, Venturelli G, Green DH, Toscani L (1987) The ultrapotassic rocks: characteristics, classification and constraints for petrogenetic models. Earth Sci Rev 24:81–134

Foley S (1992a) Petrological characterization of the source components of potassic magmas: geochemical and experimental constraints. Lithos 28:187–203

Foley S (1992b) Vein-plus-wall-rock melting mechanisms in the lithosphere and the origin of potassic alkaline magmas. Lithos 28:435–453

Fudali RF (1963) Experimental studies bearing on the origin of pseudoleucite and associated problems of alkalic rock systems. Geol Soc Am Bull 74(109):1101–1126

Gaeta M, Freda C, Christensen JN, Dallai L, Marra F, Karner DB, Scarlato P (2006) Time-dependent geochemistry of clinopyroxene from the Alban Hills (Central Italy): clues to the source and evolution of ultrapotassic magmas. Lithos 86:330–346

Gaspar JC, Wyllie PJ (1982) Barium phlogopite from the Jacupiranga carbonatite. Brazil Am Mineral 67:997–1000

Gittins J, Fawcett JJ, Brooks CK, Rucklidge JC (1980) Intergrowths of nepheline-potassium feldspar and kalsilite-potassium feldspar: a re-examination of the pseudo-leucite problem. Contrib Mineral Petrol 73:119–126

Guillou H, Scao V, Nomade S, Platevoet B, Blamart D (2017) De la justesse des âges K-Ar : exemple de la datation de deux dômes trachytiques du Gölcük (Turquie). Quaternaire 28(2):141–148

Gupta AK, Chattopadhyay S, Chattopadhyay B, Arima M (2006) Experimental Study of the system diopside-nepheline-sanidine at 0.1, 1 and 2 GPa [P($_{H2O}$)=P ($_{Total}$)]: its significance in the genesis of alkali-rich basic and ultrabasic rocks. Lithos 86:91–109

Gupta AK, Yagi K (1980). Petrology and genesis of leucite-bearing rocks, Springer-Verlag, 252.

Gupta AK (2015). Origin of potassium-rich silica-deficient igneous rocks. Springer-Verlag, 450.

Guo P, Niu Y, Yu X (2014) A synthesis and new perspective on the petrogenesis of kamafugites from West Qinling, China, in the global context. J Asian Earth Sc 79:86–96

Gürsu S, Göncüoğlu MC, Bayhan H (2004) Geology and geochemistry of the Pre-early Cambrian rocks in the Sandıklı Area: implications for the Pan-African evolution of NW Gondwanaland. Gondwana Res 7(4):923–935

Holness MB, Vernon RH (2014). The influence of interfacial energies on igneous microstructures. In: Charlier BLA, Namur O, Latypov RM, Tegner C (eds). Layered intrusions. Dordrecht Springer, 183–228.

Holness MB, Vukmanovic Z, Mariani E (2017) Assessing the role of compaction in the formation of adcumulates: a microstructural perspective. J Petrol 58:643–674

Holness MB, Clemens JD, Vernon RH (2018) How deceptive are microstructures in granitic rocks? Answers from integrated physical theory, phase equilibrium, and direct observations. Contrib Mineral Petrol 173(8):2–18

Irvine TN (1980) Magmatic infiltration metasomatism, double-diffusive fractional crystallization and adcumulus growth in the Muskox and other layered intrusions. In: Hargraves RB (ed) Physics of magmatic processes. Princeton University Press, Princeton, pp 325–383

Kampunzu AB, Lubala RT (1991). Magmatism in extensional structural settings: the Phanerozoic African Plate. Springer, 637.

Koçyiğit A (1984a) Güneybatı Türkiye ve yakın dolayında levha içi yeni tektonik gelişim. Türkiye Jeoloji Bülteni 27:1–16

Koçyiğit A (1984b). Tectono-stratigraphic characteristics of Hoyran Lake region (Isparta Bend). In: Tekeli O, Göncüoğlu MC (eds).

Geology of the Taurus Belt. Proceedings of the International Symposium held by the Mineral Research and Exploration Institute, 26–29 September 1983, 53–67, Ankara, Turkey.

Keller J (1983) Potassic lavas in the orogenic volcanism of the Mediterranean area. J Volc Geotherm Res 18:321–335

Lacroix A (1893) Les enclaves des roches volcaniques. Mâcon Protal 1(8):770

Lacroix A (1917) Les roches grenues d'un magma leucitique étudiées à l'aide des blocs holocristallins de la Somma. C R Acad Sc Paris 165:481–487

Laporte D, Provost A (2000) Equilibrium geometry of a fluid phase in a polycrystalline aggregate with anisotropic surface energies: dry grain boundaries. J Geophys Res 105:25937–25953

Larsen LM (1976) Clinopyroxenes and coexisting mafic minerals from the alkaline Ilimaussaq intrusion, South Greenland. J Petrol 12:303–315

Laval M, Hottin AM (1992) The Mlindi ring structure. An example of an ultrapotassic pyroxenite to syenite differentiated complex. Geol Rundschau 81:737–757

Lee WJ, Wyllie PJ (1998) Processes of crustal carbonatite formation by liquid immiscibility and differentiation, elucidated by model systems. J Petrol 39:2005–2013

Lefèvre C, Bellon H, Poisson A (1983) Occurrence of leucitites among the Pliocene volcanics of Isparta (Western Taurides, Turkey). C R Acad Sci II 297:367–372

Le Maitre RW (2002) Igneous rocks, a classification and glossary of terms, 2nd edn. Cambridge Univ, Press, p 236

Mansker WL, Ewing RC, Keil K (1979) Barian-titanian biotites in nephelinites from Oahu. Hawaii Am Mineralogist 64:156–159

Marsh BD (1998) On the interpretation of crystal size distributions in magmatic systems. J Petrol 39:553–599

Marsh BD (2007) Crystallization of silicate magmas deciphered using crystal size distributions. J Am Ceram Soc 90:746–757

McBirney AR (1984). Igneous petrology. Freeman, Cooper and Co. eds. 504.

McBirney AR (2007) Constitutional zone refining of layered intrusions. In: Parsons I (ed) Origins of igneous layering. Reidel, Boston, pp 437–452

McBirney AR, Boudreau AE, Marsh B (2009) Comments on "Textural maturity of cumulates: a record of chamber filling, liquidus assemblage, cooling rate and large-scale convection in mafic layered intrusions" and "a textural record of solidification and cooling in the Skaergaard Intrusion, East Greenland." J Petrol 50:93–95

Mitchell RH (2005) Carbonatites and carbonatites and carbonatites. Can Mineral 43:2049–2068

Mitchell RH, Bell K (1976) Rare earth element geochemistry of potassic lavas from the Birunga and Toro-Ankole regions of Uganda. Africa Contrib Mineral Petrol 58:293–303

Mitchell RH, Bergman SC (1991) Petrology of lamproites. Plenum Press, New York, p 456

Mitchell RH, Platt RG (1978) Mafic mineralogy of ferroaugite syenite from the Coldwell alkaline complex, Ontario. Canada J Petrol 19(4):627–651

Mitchell RH, Platt RG (1982) Mineralogy and petrology of nepheline syenites from the Coldwell alkaline complex, Ontario. Canada J Petrol 23:186–214

Mitchell RH, Vladykin NV (1996) Compositional variation of pyroxene and mica from the Little Murun ultrapotassic complex, Aldan Shield. Russia Min Mag 60(403):907–925

Peccerillo A, Poli G, Tolomeo L (1984) Genesis, evolution and tectonic significance of K-rich volcanics from the Alban Hills (Roman comagmatic region) as inferred from trace element geochemistry. Contrib Mineral Petrol 86:230–240

Peccerillo A (1990) On the origin of the Italian potassic magmas - comments. Chem Geol 85(1–2):183–191

Peccerillo A (1992) Potassic and ultrapotassic rocks: compositional characteristics, petrogenesis, and geologic significance. Episodes 15(4):243–251

Peccerillo A (1994) Mafic ultrapotassic magmas in Central Italy : geochemical and petrological evidence against primary magmas. Miner Petrogr Acta V(XXXVII):229–245

Peccerillo A, Foley S (eds) (1992). Potassic and ultrapotassic magmas and their origin. Lithos, 28, 3-6, 453.

Perini G, Conticelli S (2002) Crystallization conditions of leucite-bearing magmas and their implications on the magmatological evolution of ultrapotassic magmas: the Vico Volcano, Central Italy. Miner Petrol 74:253–276

Platevoet B, Elitok Ö, Guillou H, Bardintzeff JM, Yağmurlu F, Nomade S, Poisson A, Deniel C, Özgür N (2014) Petrology of Quaternary volcanic rocks and related plutonic xenoliths from Gölcük volcano, Isparta Angle, Turkey: Origin and evolution of the high-K alkaline series. J Asian Earth Sc 92:53–76

Platevoet B, Scaillet S, Guillou H, Blamart D, Nomade S, Massault M, Poisson A, Elitok Ö, Özgür N, Yagmurlu F, Yilmaz K (2008) Pleistocene eruptive chronology of the Gölcük volcano, Isparta Angle, Turkey. Quaternaire 19(2):147–156

Pouclet A (1980) Contribution à la systématique des laves alcalines, les laves du rift de l'Afrique Centrale (Zaïre-Uganda). Bull Volcanol 43(3):527–540

Prelević D, Foley SF, Romer RL, Cvetković V, Downes H (2005) Tertiary ultrapotassic volcanism in Serbia: constraints on petrogenesis and mantle source characteristics. J Petrol 46:1443–1487

Prelević D, Foley SF, Romer RL, Conticelli S (2008) Mediterranean Tertiary lamproites derived from multiple source components in postcollisional geodynamics. Geoch Cosmoch Acta 72:2125–2156

Prelević D, Akal C, Romer RL, Foley SF (2010a) Lamproites as indicators of accretion and/or shallow subduction in the assembly of South-western Anatolia. Turkey, Terra Nova 22(6):443–452

Prelević D, Foley SF, Stracke A, Romer RL, Conticelli S (2010b) Hf isotope compositions of Mediterranean lamproites: mixing of melts from asthenosphere and crustally contaminated mantle lithosphere. Lithos 119:297–312

Prelević D, Akal C, Foley SF, Romer RL, Stracke A, van den Bogaard L (2012) Ultrapotassic mafic rocks as geochemical proxies for postcollisional mantle dynamics of lithosphere: the case of SW. Anatolia-Turkey J Petrol 53:1019–1105

Prelević D, Akal C, Romer RL, Mertz-Kraus R, Helvaci C (2015) Magmatic response to slab tearing: constraints from the Afyon Alkaline Volcanic Complex, Western Turkey. J Petrol 56(3):527–562

Ridolfi F, Renzulli A, Macdonald R, Upton BGJ (2006) Peralkaline syenite autoliths from Kilombe volcano, Kenya Rift Valley: evidence for subvolcanic interaction with carbonatitic fluids. Lithos 91:373–392

Sahama TG (1974) Potassium rich-rocks. In: Sorensen H (ed) Alkaline rocks. Wiley, London, U.K., pp 96–109

Savasçin MY, Birsoy R, Dag N, Nohutçu E (1994) Kirka-Afyon-Isparta structural trend and Alkaline rock associations (Anatolia). Bull Geol Soc Greece VXXX(3):89–98

Savaşçin MY, Oyman T (1998) Tectonomagmatic evolution of alkaline volcanics at the Kirka-Afyon-Isparta structural trend. SW Turkey Turk J Earth Sci 7:201–214

Schönenberger J, Marks M, Wagner T, Markl G (2006) Fluid-rock interaction in autoliths of agpaitic nepheline syenites in the Ilímaussaq intrusion, South Greenland. Lithos 91:331–351

Seifert W, Kämpf H (1994) Ba-enrichment in phlogopite of a nephelinite from Bohemia. Eur J Mineral 6:497–502

Simonetti A, Bell K (1994) Nd, Pb and Sr isotopic data from the Napak carbonatite-nephelinite centre, eastern Uganda: an example of open-system crystal fractionation. Contrib Mineral Petrol 115:356–366

Sparks RSJ, Huppert HE, Kerr RC, McKenzie DP, Tait SR (1985) Postcumulus processes in layered intrusions. Geol Mag 122:555–568

Solovova IP, Girnis AV, Rass IT, Keller J, Kononkova NN (2003) Different styles of evolution of CO2-rich alkaline magmas: the role of melt composition in carbonate-silicate liquid immiscibility. Per Mineral Eurocarb Workshop Spec Issue 1(LXXII):87–93

Stoppa F (2003) Consensus and open questions about Italian CO_2-driven magma from the mantle. Per Mineral Eurocarb Workshop Special Issue 1(LXXII):1–8

Stoppa F, Cundari A, Rosatelli G, Wooley AR (2003) Leucite melilitolites in Italy: genetic aspects and relationships with associated alkaline rocks and carbonatites. Per Mineral Eurocarb Workshop Special Issue 1(LXXII):223–251

Stoppa F, Rosatelli G, Wall F, Le Bas MJ (2003) Texture and mineralogy of tuffs and tuffisites ar Ruri volcano in western Kenya: a carbonatite, melilite, mantle-debris trio. Per Mineral Eurocarb Workshop Special Issue 1(LXXI):181–204

Stoppa F, Loyd EL, Rosatelli G (2003) CO2 as the propellant of carbonatite-kamafugite cognate pairs and the eruption of diatremic tuffisite. Per Mineral Eurocarb Workshop Special Issue 1(LXXII):205–222

Sun SS, McDonough W (1989) Chemical and isotopic systematics of oceanic basalts: implications for mantle composition and processes In: Saunders AD, Norry MJ (eds) Magmatisms in the oceanic basins. Geol Soc London Spec Publ 42(1):313–345

Tait SR, Huppert HE, Sparks RSJ (1984) The role of compositional convection in the formation of adcumulate rocks. Lithos 17:139–146

Tappe S, Foley SF, Pearson DG (2003) The kamafugites of Uganda: a mineralogical and geochemical comparison with their Italian and Brazilian analogues. Per Mineral Eurocarb Workshop Special Issue 1(LXXII):51–77

Tuttle OF, Smith JV (1958) The nepheline-kalsilite system; II, Phase relations. Amer J Sci 256:571–589

Thornton CP, Tuttle OF (1960) Chemistry of igneous rocks. I: the differentiation index. Amer J Sci 258:664–684

Veksler IV, Fedorchuk YM, Nielsen TFD (1998) Phase equilibria in the silica-undersaturated part of the KalSiO4 – Mg2SiO4 – Ca2SiO4 – SiO2 – F system at 1 atm and the larnite-normative trend of melt evolution. Contrib Mineral Petrol 151:347–363

Vollmer R (1989) On the origin of the Italian potassic magmas: 1. Discus Contrib Chem Geol 74(3–4):229–239

Wagner C, Velde D (1986) The mineralogy of K-richterite-bearing lamproites. Am Mineral 71:17–37

Wagner C, Velde D, Mokhtari A (1987) Sector zoned phlogopites in igneous rocks. Contrib Mineral Petrol 96:186–191

Woolley AR (2003) Igneous silicate rocks associated with carbonatites: their diversity, relative abundances and implications for carbonatite genesis. Per Mineral Eurocarb Workshop Special Issue 1(LXXII):9–17

Woolley AR, Bergman SC, Edgar AD, Le Bas MJ, Mitchell RH, Rock NMS, Scott-Smith BH (1996) Classification of lamprophyres, lamproites, kimberlites, and the kalsilitic, melilitic, and leucitic rocks. Can Mineral 34:175–186

Yağmurlu F, Savaşçin MY, Ergün M (1997) Relation of the alkaline volcanism and active tectonism within the evolution of the Isparta angle, SW Turkey. J Geol V105:717–728

Yoder HS (1986) Potassium-rich rocks: phase analysis and heteromorphic relations. J Petrol 27(5):1215–1228

Zeng RS, MacKenzie WS (1984) Preliminary report on the system $NaAlSiO_4$-$KAlSiO_4$-SiO_2-H_2O at P_{H2O} = 5 kbar. Bull Minéral 107:571–577